ABSTRACT

Title of Thesis:	BRITTLE FAULTING IN POROUS, WATER-SATURATED SANDSTONE DEFORMED UNDER HIGH PORE FLUID PRESSURE
	Zachary Zega, Master of Science, 2020
Thesis Directed By:	Professor Wenlu Zhu, Department of Geology

The effective stress law is widely used to model the deformation of crustal rock. It states that effective pressure, the difference between confining pressure and pore fluid pressure, dictates rock strength. In low-porosity rock, previous work has shown that the stability of faulting is controlled by the magnitude of pore fluid pressure rather than the effective pressure. To understand the effect of pore fluid pressure on porous rocks, I deformed water-saturated samples of Darley Dale Sandstone (~13-15% initial porosity) at strain rates from 10^{-4} to 10^{-6} s^{-1} while using a constant effective pressure of 10 MPa and pore fluid pressures ranging from 2 to 180 MPa. The results show that the shear strength is well-predicted by the effective stress law, but fault growth at P_f = 180 MPa resulted in pervasive grain comminution and stabilized fault propagation compared to all other lower pressure experiments.

BRITTLE FAULTING IN POROUS, WATER-SATURATED SANDSTONE DEFORMED UNDER HIGH PORE FLUID PRESSURE

by

Zachary J Zega

Thesis submitted to the Faculty of the Graduate School of the
University of Maryland, College Park, in partial fulfillment
of the requirements for the degree of
Master of Science
2020

Advisory Committee:
Professor Wenlu Zhu, Chair (University of Maryland)
Professor Laurent Montesi (University of Maryland)
Assistant Professor Mong-Han Huang (University of Maryland)

Table of Contents

List of Tables

List of Figures

Chapter 1: Introduction

1.1: Motivation and Geological Context

As originally proposed in 1910, elastic rebound theory models the earthquake cycle as having the interseismic period of steady strain accumulation and the coseismic period of sudden strain release along a tectonic fault that results in an earthquake (Reid, 1910). Since the mid-twentieth century, geodetic measurements of crustal movement have revealed more complex patterns of fault movement during the seismic cycle (i.e. Scholz, 1972). Slow slip events, an example of one such complexity, describe fault movement that is faster than the average plate velocity but slower than a normal earthquake (Peng and Gomberg, 2010; Bilek and Lay, 2018).

The largest earthquakes on earth occur at subduction zone megathrusts, but multiple types of fault slip have been observed at subduction zones (Figure 1). For instance, a fault may creep without producing seismic waves (aseismic creep), slip slowly and propagate low-frequency seismic energy (episodic tremor and slow slip), or slip unstably as in a normal earthquake (rapid stick-slip movement) (Peng and Gomberg, 2010; Bilek and Lay, 2018). Compared to earthquakes, slow slip events have a longer duration, slower slip rate, and smaller stress drop, and they can sometimes be observed both before and after major subduction zone megathrust earthquakes (Kato et al., 2012; Uchida et al., 2015; Bilek and Lay, 2018). Observations of slow slip events at subduction zones have suggested that the occurrence of slow slip events prior to megathrust earthquakes reduces seismic hazard by relieving stress while other data suggest that slow slip events may trigger

larger earthquakes through stress transfer (see Radiguet, 2012; Koulali, 2017; Reyners and Bannister, 2007). Because slow slip events occur both before and after some catastrophic earthquakes, they are a crucial part of the seismic cycle. However, exactly how slow slip events may contribute to the initial nucleation of some earthquakes remains unknown.

Regions of slow slip along the subduction zone interface often correlate with areas of anomalously high V_p/V_s ratios, which are interpreted as zones of elevated pore fluid pressure (i.e. Shelley et al., 2006, Peacock et al., 2010, Kodaira et al., 2004). Because several seismological studies have closely associated elevated pore fluid pressure with slow slip, the presence of high pore fluid pressure is thought to promote tremor, low frequency events, and aseismic creep at subduction zones (Tobin and Saffer, 2009; Figure 1). In addition to the abundant amount of seismological data that suggests the presence of elevated pore fluid pressure along subduction zone interfaces, sophisticated borehole measurements along the seaward portion of certain subduction zone forearcs have correlated transient changes in in-situ pore pressure measurements with geodetically inferred slow slip events (Solomon et al., 2009). Additionally, the hypocenters of low-frequency events located approximately 10 km below the trench axis commonly coincide with areas that are inferred to have low effective stress and high pore fluid pressure (Kitajama and Saffer, 2012; Figure 1). Taken together, this evidence strongly suggests pore fluid pressure controls the style of slip along subduction zone interfaces (Figure 1).

At shallow depths in earth's crust, rocks fail by brittle faulting or frictional sliding when the shear stress reaches a critical value of shear stress (τ_c) (e.g., Paterson

and Wong, 2005). The failure criterion (i.e., Mohr-Coulomb criterion) is given by $\tau_c = \mu(\sigma_n') + \tau_o$ where μ is the coefficient of internal friction, τ_o represents the rock's cohesive strength, and the effective normal stress (σ_n') is equal to the normal stress (σ_n) minus the pore fluid pressure (P_f) (i.e. $\sigma_n' = \sigma_n - \alpha P_f$ where $\alpha \approx 1$ for brittle deformation). According to the effective stress law (Terzaghi, 1943), increasing pore fluid pressure reduces the effective normal stress and lowers the critical shear stress, which means failure will occur at a lower shear stress along a given plane. The Mohr-Coulomb failure criterion predicts that a rock will fail when the shear stress exceeds a threshold value; however, it does not provide any information on whether the subsequent fault growth or frictional sliding is stable (slow slip) or unstable (dynamic rupture).

To date, the mechanical link between high pore fluid pressure and slow slip behavior is not well understood. How does high pore fluid pressure impede fault motion? What are the underlying mechanical mechanisms? These are important questions to address in order to gain a better understanding of slow slip events at subduction zones.

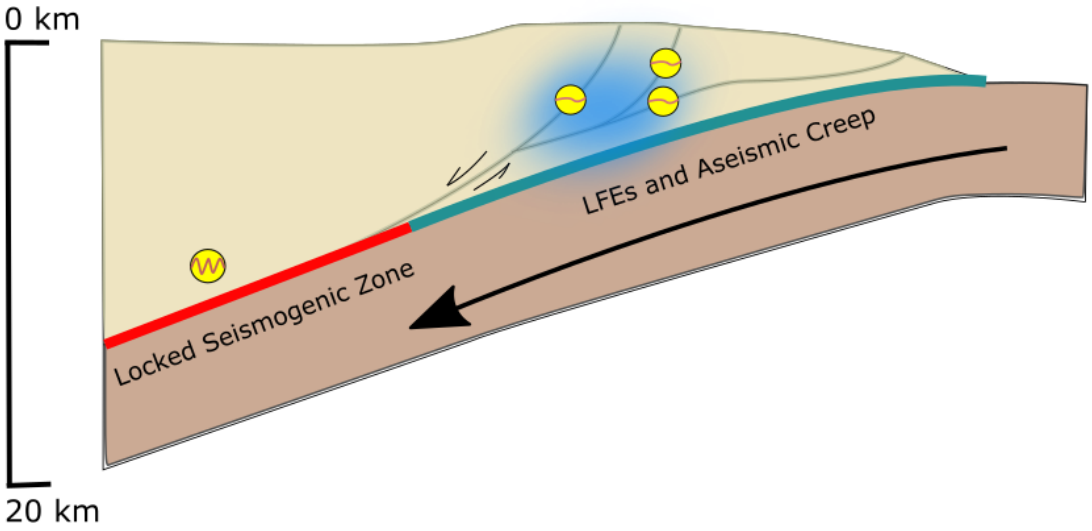

Figure 1: A schematic depicting the effect of elevated pore fluid pressure on slip behavior in the outer wedge of a subduction system (following Tobin and Saffer (2009)).The incoming plate entrains wet sediments and hydrous minerals into the accretionary prism of the overriding plate, which causes a zone of high pore fluid pressure and low effective pressure (outlined with a blue cloud) (Tobin and Saffer, 2009). Whether or not high pore fluid pressure is localized along the plate interface or more pervasive throughout the entire accretionary wedge remains unknown (Saffer and Tobin, 2012). The zone of highest pore fluid pressure is collocated with low frequency event hypocetners (circled low amplitude sine waves). Further down-dip, the fluids progressively drain and cause an increase in effective pressure and a transition toward higher plate coupling. Higher effective pressure coincides with the occurrence of major earthquakes (higher amplitude circled sine wave).

1.2: Time-Dependent Effects in Deforming Rock

In the brittle regime, rocks deform quasi-elastically until they reach a yield point. At the onset of yielding, rocks dilate due to tensile microcracking and deform inelastically until failure (Brace et al., 1966; Reches and Lockner, 1994; Wong et al., 1997). When fluid is present in rocks, there are various time-dependent effects that can influence both the elastic and inelastic response of a deforming rock sample (Rice, 1975; Baud et al., 2000; Makhneneko and Labuz, 2015). Two end-member time scales are used to describe deformation in fluid-saturated rocks: the drained case and the undrained case. In the undrained case, cracks open at a rate that is faster than the rate of fluid diffusion to the newly created void space (Rice, 1975; Figure 2). In the drained case, cracks open at a rate that is slower than or equal to the time required

for fluid to diffuse to the newly created void space (Rice, 1975; Figure 2). In the undrained case, the effective normal stress at the crack tip is higher compared to the drained case due to lower pore fluid pressure present at the crack tip (Rudnicki and Chen, 1988; Rice, 1975). Because the effective normal stress increases at the crack tip and a higher value of shear stress is needed for the crack to grow, the undrained condition results in a phenomenon known as dilatant hardening, which describes an underlying process that impedes failure in fluid saturated brittle materials (Rice, 1975). Ultimately, the presence of pore fluid in rocks introduces a time-dependent competition between the rate of crack growth and fluid diffusion into newly created void space that results in mechanical behavior characteristic of either a drained or undrained case (i.e. Rudnicki, 1984). Using a mathematical approach, Rudnicki and Chen (1988) were the first to demonstrate that dilatant hardening may inhibit dynamic rupture in rocks under axisymmetric loading when the pore fluid pressure exceeds a threshold value (Figure 2 bottom).

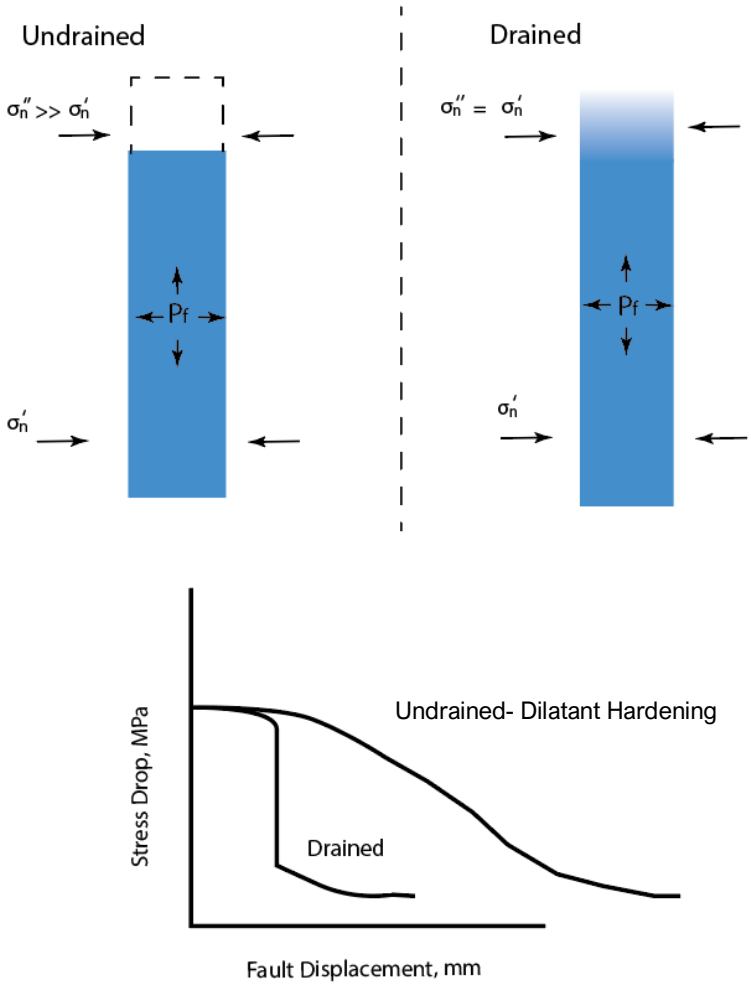

Figure 2: (Top) Distinguishes the drained and undrained conditions. In the undrained condition, the effective normal stress on the crack tip (σ_n'') is higher than in the drained condition where fluid can drain to the crack tip. The effective normal stress on the pre-existing crack is represented as (σ_n'**)** (Bottom) The undrained condition, which leads to dilatant hardening, causes stabilized slip weakening behavior (following Rudnicki and Chen, 1988).

Laboratory experiments have shown that, for the same effective pressure, conditions of high pore fluid pressure reduce the rate of fault propagation in compact rocks (initial porosity < 1%) (Martin, 1980; French and Zhu, 2017). Martin (1980) performed a series of constant strain rate experiments while maintaining the same value of effective pressure (i.e., confining pressure minus pore fluid pressure) and

demonstrated that fault propagation in Westerly Granite transitioned from unstable to stable when the pore fluid pressure exceeded a critical value. More recently, French and Zhu (2017) also conducted a series of experiments in which they increased pore fluid pressure while maintaining a constant effective pressure and found that fault propagation was stabilized at high pore fluid pressures in serpentinite. The mechanical data documented in experiments by Martin (1980) and French and Zhu (2017) align with the dilatant hardening conceptual framework as it is theoretically described by Rudnicki and Chen (1988) (Figure 2).

The stabilized fault propagation observed in French and Zhu (2017) may have occurred because the serpentinite used in the study had low initial porosity and bulk permeability. Compact rocks with low permeability are more susceptible to dilatant hardening because they are likely to exhibit an undrained mechanical response unless the deformation rate is slow. In other words, pore fluid diffuses to open void spaces over a much longer timescale in compact rock with low permeability when compared to porous rocks with higher permeability. For example, Brace and Martin (1968) found that the effective stress law was valid for Westerly Granite only when the strain rate was decreased to 10^{-7} s^{-1} or lower, which suggests that the rock only exhibited a drained mechanical response once it was deformed at a slow strain rate $\leq 10^{-7}$ s^{-1}. In comparison to Westerly Granite, Brace and Martin (1968) found Pottsville sandstone only exhibited a strength increase due to undrained deformation at a much higher strain rate of 10^{-4} s^{-1}, which suggests that the pore fluid pressure equilibrated at faster rates in Pottsville sandstone samples compared to Westerly granite samples. French and Zhu (2017)'s detailed microstructural analysis showed that failure is localized at

low pore fluid pressure conditions but the stress-induced fractures become increasingly distributed at high pore fluid pressures—an observations that suggests microcracks were impeded by locally high effective stresses which resulted in the observed slow slip behavior and distributed deformation.

The presence of pore fluid also introduces other time-dependent phenomenon besides the previously outlined drainage effects. For instance, pore fluid can weaken rocks by stress corrosion (e.g., Anderson & Grew, 1977; Baud et al., 2000). Strained Si-O bonds in silicate-rich rocks may react with the interstitial aqueous fluid to form a hydrolyzed Si-OH bond that can be broken at lower stresses than the Si-O bond; this chemical process can allow rocks to deform below their short-term failure strength (Atkinson, 1984; Baud et al., 2000; Heap, 2009). For example, fluid-saturated rocks in the brittle regime that are kept at a constant differential load above their yield strength deform by brittle creep where the strain rate is variable with time and the rock sample fails in a nearly identical manner to a rock deformed at a constant strain rate (Baud et al., 1997; Heap et al., 2009; Brantut et al., 2014). Additionally, evidence for stress corrosion and "water-weakening" effects can be observed during constant strain rate experiments. For example, Duda and Renner (2013) observed a systematic decrease in both yield and brittle failure strengths as a result of decreasing the strain rate from $10^{-3}s^{-1}$ to $10^{-7}s^{-1}$. Typically, stress corrosion cracking is thought to be the main mechanism for brittle creep at shallow crustal depths and is recognized as playing a critical role in deformation of earth's crust.

1.3: Research Goals

In nature, fluid cycling at faults has been found to be an important controlling factor governing their long-term strength (Sibson, 1992). So-called "fault-valve" behavior describes cyclical fault weakening due to rises in pore fluid pressure and subsequent fault strengthening after the drainage of pore fluid. Enhanced fault roughness results in higher permeability of the fault zone in the time following rupture, and subsurface processes such as hydrothermal precipitation have been found to heal faults and decrease their permeability over time (Sibson, 1992). Due to the variable porosity, permeability, and fluid pressures present at active faults overtime, understanding failure behavior in fluid-saturated, porous rocks in addition to compact rocks is critical. The primary goal of the research presented here is to contribute both mechanical data and microstructural observations that describe the behavior of porous rocks at various strain rates and pore fluid pressures and to better understand the effects of pore fluid pressure and strain rate on fault growth during brittle failure.

Most work investigating the effect of pore fluid pressure on brittle faulting in porous rock revolves around increasing the strain rate to impose an undrained condition. According to Brace and Martin (1968), a certain critical strain rate should exist, and if a given rock is deformed faster than the critical strain rate, dilatant hardening can occur because there is only a short time scale allowed for drainage of the pore fluid. For instance, Lei et al. (2011) demonstrated that the peak strength of Berea Sandstone increased by ~30% when the strain rate was increased to $10^{-3}s^{-1}$. Duda and Renner (2013) performed constant strain rate experiments on various sandstones to approximate drained and undrained conditions, and they observed a

significant increase in peak strength in their rocks deformed at a strain rate of $10^{-3}s^{-1}$ compared to experiments conducted at $10^{-7}s^{-1}$. Other studies have used different experimental approaches to investigate the effect of pore fluid pressure on porous rocks. For instance, Ougier-Simonin and Zhu (2013 and 2015) showed that increasing pore fluid pressure prior to sample failure does not significantly alter the failure behavior of Darley Dale and Berea sandstones in the brittle faulting regime. Makhnenko and Labuz (2015) were able to observe dilatant hardening in Berea sandstone by completing an undrained deformation experiment where pore fluid was pumped into the sample but not allowed to flow out during the entirety of deformation. This was accomplished by imposing pore fluid pressure in the sample and then isolating both the upstream and downstream fluid reservoirs such that the mass of fluid within the sample was held constant during deformation (undrained condition). Makhnenko and Labuz (2015) found that the undrained experiment led to higher shear strength of Berea sandstone compared to drained experiments where both upstream and downstream pore fluid reservoirs were left open. Most mechanical data for fluid-saturated porous rocks suggests that increasing the strain rate should impose an increasingly undrained condition and lead to an increase in peak strength of the rock. However, the current literature does not link conditions of elevated pore fluid pressure to stabilized fault propagation in porous rocks.

In this study, I conducted laboratory experiments and a microstructural analysis in order to investigate if there is a relationship between slow fault propagation and high pore fluid pressure in porous rocks. Fluid-saturated samples of Darley Dale Sandstone were deformed at strain rates from $10^{-4}\,s^{-1}$ to $10^{-6}\,s^{-1}$, at a

constant effective pressure of 10 MPa, with confining pressures ranging from 12 to 190 MPa, and pore fluid pressures ranging from 2 to 180 MPa. This work complements earlier work by French and Zhu (2017) and Martin (1980) by investigating the effect of high pore fluid pressure on porous rocks rather than compact rocks. Additionally, by varying the strain rate, other important rate-dependent effects such as subcritical crack growth and water-weakening effects can be discerned from the microstructural and mechanical data in samples that were deformed at fast versus slow rates (see Atkinson, 1984 and Baud et al., 2000 for more details). Also, mosaics of photomicrographs were created for end-member samples deformed at pore fluid pressures of 2 MPa and 180 MPa. By examining the damage produced in both samples, the specific mechanical effects of high pore fluid pressure on faulting in porous rock can be discerned from a rock deformed at low pore fluid pressure.

1.4: Research Hypotheses

The effective stress law is the main theoretical framework used to assess the effect of pore fluid pressure on rocks, but for a constant effective pressure, the absolute value of pore fluid pressure has been found to influence the style of faulting in rocks (i.e. French and Zhu 2017; Martin, 1980). Dilatant hardening should only occur when effective drainage cannot be maintained within a deforming rock and there are correspondingly local increases in effective normal stresses on crack tips. The local increases in effective pressure could clamp crack tips and prevent them from unstably propagating (French and Zhu, 2017). French and Zhu (2017) argue that

samples deformed at high pore fluid pressures will experience higher local clamping due to higher confinements and thus cause fault nucleation and propagation to migrate (become more distributed) when the local effective normal stress becomes too high to allow for further deformation in a certain region of the sample. French and Zhu (2017) do not answer the scientific questions of whether such effects can occur in porous rocks.

This study maintains a focus on fault propagation and whether there is any relationship between the loading rate, pore fluid pressure, and the observed rate of fault propagation in the laboratory. Along the subduction zone interface, the style of slip behavior is mediated by the magnitude of pore fluid pressure (Figure 1). The confining and pore fluid pressures that are achieved in this study can be related to the pressure conditions of the top ~10 km of the subduction zone forearc where there is high pore fluid pressure and low effective pressure (Figure 1). At this location, abundant low frequency events often coincide with a zone of anomalously high pore fluid pressure. In this laboratory study, I couple mechanical data with microstructural observations to investigate the link between high pore fluid pressure and slow fault propagation. The data presented here can help determine what micromechanical mechanisms at high pore fluid pressure result in slow slip behaviors as they are observed in nature (Figure 1).

Chapter 2: Methodology

2.1: Sample Material: Darley Dale Sandstone

Darley Dale Sandstone is as an indurated, feldspathic sandstone found in Derbyshire, England and was used to gather all the mechanical and microstructural

data presented in this study. Heap (2009) reported a modal composition for Darley Dale Sandstone of 69% quartz, 26% feldspar, 3% clay, and 2% mica. I determined the average spherical grain diameter by following Underwood (1969) and using the following formula:

$$D = \frac{6 * L_3}{4}$$

Here, D is the estimated grain diameter, and L_3 is the mean intercept length: the number of grain intercepts per unit length of test line observed in thin section (i.e. Table 2.2, Column A in Underwood, 1969). Following this procedure and measuring the number of grains per unit test line for 100 separate transects, I determined a grain diameter of 0.29 mm ± 0.16 mm (two standard deviations). For reference, Wong et al., (1997) reported an estimated grain diameter of 0.34 mm.

Initial porosities of the samples used in this study varied between 13.1 % to 15.6% (Table 1). The measurement of initial porosity in samples varies roughly 1% primarily because the soaked weight of the sample is difficult to consistently determine with the method used. Permeability measurements were not conducted during the experiments shown here, but the permeability of Darley Dale is ~10^{-14} m^2 (Zhu and Wong, 1997). Previous work using Darley Dale Sandstone has focused on a variety of material properties and behaviors such as time-dependent brittle creep, mechanical compaction, the water weakening effect, and permeability evolution (see Heap et al., 2009; Baud, 2000; Baud and Meredith, 1997; Wong et al., 1997; Zhu and Wong, 1997). Additionally, detailed microstructural work on Darley Dale Sandstone was completed by Wu et al. (2000). Because of the abundance of pre-existing mechanical and microstructural data, the material properties of Darley Dale

Sandstone at a variety of conditions are well-known, and the data shown here can be compared to prior publications.

2.2: Sample Preparation

All samples of Darley Dale Sandstone were cored perpendicular to bedding from two separate blocks and cut into right cylinders with diameters of 18.41 mm (0.725 inch) and lengths of 38.10 mm (1.5 inches), or diameters of 25.40 mm (1 inch) and lengths of 50.8 mm (2 inches). All sample lengths and diameters were measured in triplicate to ensure the proper dimensions and then were dried in a heated vacuum oven for 24 hours at 60˚ C. After weighing each dried sample three times, the samples were then saturated in deionized water vapor before being placed in a vacuum and submerged in deionized water for an additional 24 hours. After the 24-hour saturation period, the saturated samples were each weighed three times (Table 1). To obtain initial sample porosity, the pore volume was determined from the difference between the average saturated and dried sample weight and divided by the total sample volume which was calculated from the samples' average length and diameter (Table 1).

The samples were kept in deionized water for ~12 hours, so they remain saturated before preparing a sample. Prior to an experiment, a sample is jacketed with a thin (0.1 mm thick) piece of copper. In order to make the copper fit tightly around the rough surface of the rock, the jacketed sample is placed under 7 MPa of confining pressure. After the jacket is fitted, the surface of the copper was sanded to allow for an axial and radial strain gauge to be affixed to the sample. The sample with strain gauges was placed between two double o-ring endcaps and a series of spacers that

were attached to a base plug that seals one end of the pressure vessel in the triaxial deformation apparatus. The sample was held in place with polyolefin heat-shrink tubing and hand-twisted 24-gauge steel tie-wires (Figure 3). Holes were added to the polyolefin jacket to allow wires from the strain gauge to be plugged into pins on the base plug. A hole was punched to connect the strain gauge wires were sealed with a room-temperature vulcanizing silicone gel to prevent leaking to the sample.

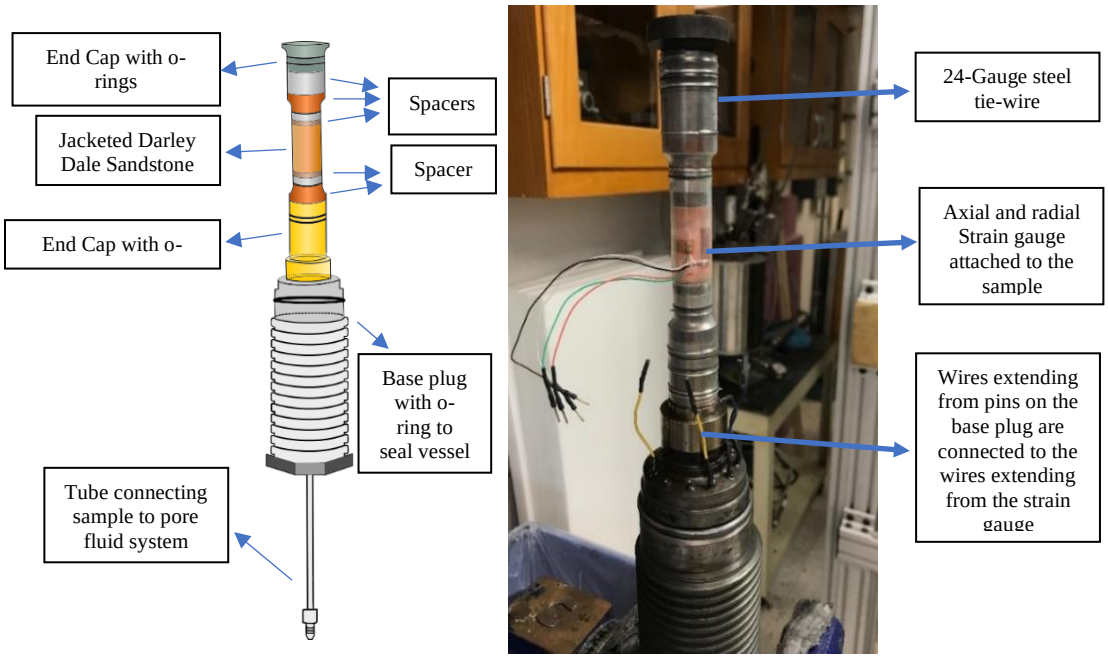

Figure 3: (Left) Shows a schematic of the base plug that is placed in the pressure vessel with each important item labelled. (Right) shows a photo of the sample with strain gauges and 24-gauge steel wire tied to the sample.

Table 1: Shows the sample ID, length measurements, diameter measurements, dry weights, and water-soaked weights used to calculate the porosity of each sample of Darley Dale sandstone that was deformed for this study. The porosity measurement may vary by up to 1.5% for a given sample (determined by using the maximum and minimum values for sample and pore volumes).

Sample ID	Length, mm	Avg. Length, mm	Diameter, mm	Avg. Diameter, mm	Dry Weight, g	Avg Dry Weight, g	Soaked Weight, g	Avg. Soaked Weight, g	Sample Volume, cm^3	Pore Vol., cm^3	Porosity, %
JU3	38.18		18.51		22.9495		24.4496				
	38.19		18.51		22.9495		24.4617				
	38.18	38.18	18.51	18.51	22.9496	22.9495	24.5029	24.4714	10.27	1.52	14.8
JU4	38.18		18.51		22.8784		24.3792				
	38.18		18.5		22.8789		24.3818				
	38.17	38.18	18.49	18.5	22.8787	22.8787	24.3816	24.3809	10.26	1.5	14.6
JU5	38.16		18.47		22.8209		24.388				
	38.14		18.48		22.821		24.3733				
	38.15	38.15	18.49	18.48	22.821	22.821	24.3662	24.3758	10.23	1.55	15.2
JU6	38.15		18.57		22.7671		24.3731				
	38.15		18.51		22.7677		24.3668				
	38.16	38.15	18.53	18.54	22.7682	22.7677	24.3756	24.3718	10.3	1.6	15.6
JU7	38.18		18.51		22.8652		24.4347				
	38.18		18.5		22.8661		24.4043				
	38.18	38.18	18.51	18.51	22.8666	22.866	24.398	24.4123	10.27	1.55	15.1
JU8	38.18		18.5		22.895		24.282				
	38.19		18.51		22.8952		24.2736				
	38.18	38.18	18.51	18.51	22.8955	22.8952	24.2567	24.2708	10.27	1.38	13.4
JU9	38.2		18.52		22.8732		24.4439				
	38.19		18.49		22.8741		24.453				
	38.2	38.2	18.51	18.51	22.8741	22.8738	24.4469	24.4479	10.27	1.57	15.3
JU10	38.2		18.52		22.889		24.4879				
	38.17		18.49		22.8894		24.4414				
	38.19	38.19	18.51	18.51	22.8893	22.8892	24.4267	24.452	10.27	1.56	15.2
JU11	38.2		18.52		22.8966		24.4749				
	38.19		18.54		22.8973		24.463				
	38.19	38.19	18.55	18.54	22.8977	22.8972	24.4832	24.4737	10.31	1.58	15.3
JU12	38.19		18.48		22.8301		24.3754				
	38.17		18.54		22.8309		24.3832				
	38.18	38.18	18.47	18.5	22.8302	22.8304	24.3424	24.367	10.26	1.54	15

D20	51.09		25.52		58.2334		61.9851				
	50.96		25.54		58.2324		61.9378				
	50.93	50.99	25.49	25.52	58.2325	58.2328	61.055	61.6593	26.08	3.43	13.1
D21	50.85		25.59		58.2137		62.0903				
	50.86		25.53		58.2135		61.9945				
	50.87	50.86	25.58	25.57	58.2125	58.2132	62.0565	62.0471	26.11	3.83	14.7
D22	50.89		25.49		58.5492		62.2021				
	50.92		26.48		58.5494		62.1732				
	50.87	50.89	25.49	25.82	58.5493	58.5493	62.0918	62.1557	26.65	3.61	13.5
D24	50.9		25.52		58.03		61.9883				
	50.85		25.51		58.0293		61.9132				
	50.84	50.86	25.56	25.53	58.0303	58.0299	61.8745	61.9253	26.04	3.9	15
D25	50.9		25.5		58.6204		62.3793				
	50.85		25.49		58.6207		62.3184				
	50.85	50.87	25.48	25.49	58.6197	58.6203	62.2777	62.3251	25.96	3.7	14.3
D26	51.01		25.5		58.4963		62.0713				
	50.86		25.49		58.4968		62.0656				
	50.94	50.94	25.48	25.49	58.497	58.4967	62.1066	62.0812	26	3.58	13.79
D29	50.88		25.49		58.1969		62.0421				
	50.91		25.48		58.197		61.9962				
	50.87	50.89	25.47	25.48	58.1972	58.197	61.9603	61.9995	25.95	3.8	14.7

2.3: Triaxial Deformation Apparatus: The Hot Press

The hot press is a servo-controlled triaxial deformation apparatus that can use argon gas or kerosene as a confining medium (Figure 4). This machine is designed to deform rocks at various confining and pore fluid pressures while a hydraulically powered and servo-controlled piston imposes an axial stress that deforms the sample at a specified displacement rate. In the experiments shown here, kerosene was used as the confining medium. For all experiments, deionized water was used as a pore fluid, and the sample was sealed, so mixing between the pore fluid (water) and confining medium (kerosene) cannot occur. The confining and pore fluid pressure were controlled with intensifiers that are filled with kerosene and water respectively. Using an analog, closed-loop servo control, the displacement of these intensifiers can advance at a constant rate to increase pressures and can be set at a specified value to maintain a constant pressure. The pore fluid and confining pressures were measured with transducers attached to the machine. The hot press can accommodate confining pressures of >200 MPa when kerosene is used and pore fluid pressure of up to 200 MPa.

2.4: *Constant Strain Rate Experiments and Loading Configuration*

After the sample was prepared and attached to the base plug, the sample was placed into the pressure vessel. An initial confining pressure of 7 MPa was applied to the sample. While the sample is under pressure, the pore fluid system was filled with water and connected to the sample. The confining pressure (P_c) was slowly raised to 20 MPa while concurrently increasing the pore fluid pressure (P_f) to 10 MPa. All experiments presented here were completed at an effective pressure (P_c -P_f) of 10

MPa. However, samples deformed at P_c =12 and P_f =2 MPa were not subject to higher pressures. Instead, pore fluid pressure (no more than 5 MPa) and confining pressure (up to 12 MPa) was introduced and the value of pore fluid pressure was then adjusted to 2 MPa using the servo-controlled pore fluid intensifier. Samples deformed at P_c = 12 and P_f = 2 MPa were left to pre-compact at P_c = 12 MPa and P_f = 2 MPa for one hour and were deformed at these pressure conditions using the outlined procedure below.

Samples deformed at higher pressures ($P_f \geq 10$ MPa) were left to to pre-compact at P_c = 20 MPa and P_f = 10 MPa for one hour. The experimental conditions of confining and pore fluid pressure were met by gradually in higher pressure experiments by increasing pressure with the pore fluid and confining pressure intensifiers while maintaining a constant effective pressure of 10 MPa. Once the pressure conditions for a given experiment were met, the hydraulic ram was used to find the point at which the piston touches the sample. The displacement of the main ram was measured with a linear variable differential transformer (LVDT), and the axial stress on the piston was measured with a force gauge placed outside the pressure vessel (Figure 5). Once the hit point was found, the ram was lowered away from the sample at a slower displacement rate to measure seal friction (the measured force due to the friction between the advancing piston and confining pressure seal assembly). Once the force gauge gave a stable reading after retracting the piston, the ram was advanced at a constant displacement rate to deform the sample. During deformation, the maximum principal stress (σ_1) increases while the intermediate and minimum principal stresses ($\sigma_2=\sigma_3 = P_c$) were kept constant. This introduced a differential stress

($\sigma_1 > \sigma_3$) (see Figure 5), which was increased until sample failed by brittle faulting. In this study, three different strain rates were investigated: 10^{-4} s^{-1}, 10^{-5} s^{-1}, and 10^{-6} s^{-1}.

All samples failed by strain softening (stress drop) and shear localization. The deformed samples were unloaded at the same strain rate as soon as the stress drop leveled off to preserved deformation microstructures. The confining and pore fluid pressures were lowered at a constant rate after the sample was unloaded and the hydraulic ram was moved away from the sample.

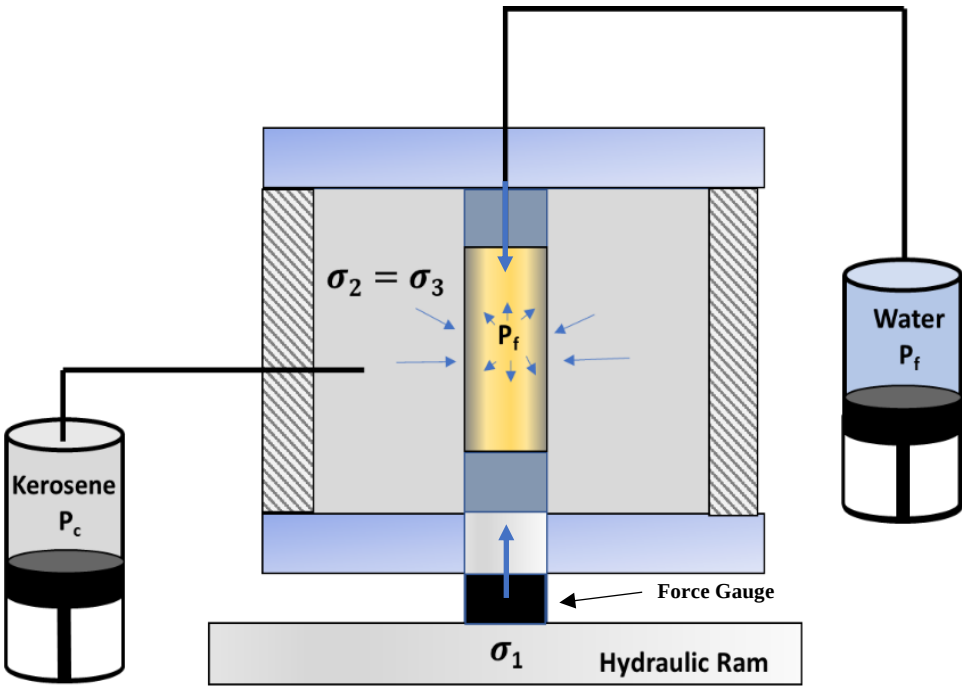

Figure 5: A simplified schematic showing the loading configuration used in all experiments presented here. The confining pressure first creates a uniform stress around the sample ($\sigma_1 = \sigma_2 = \sigma_3$) and then the pore fluid pressure (P_f) is introduced. A hydraulic ram is used to deform the sample and introduces a differential stress (i.e. $\sigma_1 > \sigma_2 = \sigma_3$). The stress applied by the ram is measured with a force gauge located outside of the pressure vessel.

Figure 4: A picture of the hot press at the University of Maryland Rock Physics Lab. To the left, there are Heise gauges that measure the pressure in the confining pressure intensifier and pressure vessel. The servo control with red digital displays can be seen on the right.

Table 2: Outlines the experimental conditions used for all experiments presented in this study. All experiments were performed at an effective pressure of 10 MPa. The sample ID refers to the samples described in Table 1.

Confining Pressure, MPa	Pore Fluid Pressure, MPa	Strain Rate, s^{-1}	Sample ID	Effective Pressure, MPa	Complete Strain Gauge Data?
12	2	10^{-6}	JU7	10	Yes
20	10	10^{-6}	D21	10	Yes
20	10	10^{-6}	D22	10	Yes
70	60	10^{-6}	JU8	10	No
130	120	10^{-6}	JU6	10	Yes
130	120	10^{-6}	D20	10	Yes
190	180	10^{-6}	JU12	10	No
12	2	10^{-5}	JU5	10	Yes
70	60	10^{-5}	JU3	10	No
130	120	10^{-5}	JU4	10	Yes
130	120	10^{-5}	D29	10	Yes
190	180	10^{-5}	JU11	10	Yes
20	10	10^{-4}	JU9	10	Yes
20	10	10^{-4}	D26	10	No
20	10	10^{-4}	D25	10	Yes
130	120	10^{-4}	D24	10	Yes
130	120	10^{-4}	J10	10	Yes

2.5: Microstructural Analysis

Visual examination of deformed samples retrieved from the pressure vessel revealed that a through-going fracture developed in all samples. These samples were dried and impregnated with low viscosity and slow cured epoxy. Each sample was then cut in half lengthwise at an orientation that maximized the surface area of the newly created plane and the fault (Figure 6). Using one half of the deformed sample,

double polished thin sections (30 microns thick) were made for the microstructural analysis. The other half was preserved for potential future studies.

Microcrack densities of deformed samples were counted from 8 separate photomicrographs that were taken on a petrographic microscope under reflected light at a total magnification of 50x. A set of 8 photographs were taken of samples JU12 (deformed at P_c = 190 MPa and P_f = 180 MPa) and JU7 (deformed at P_c = 12 MPa and P_f = 2 MPa) (Table 1; Table 2). These photos represent the same region in both samples and were intentionally taken of areas that were well-preserved along the localized shear band (see Appendix A4; Figure 6).

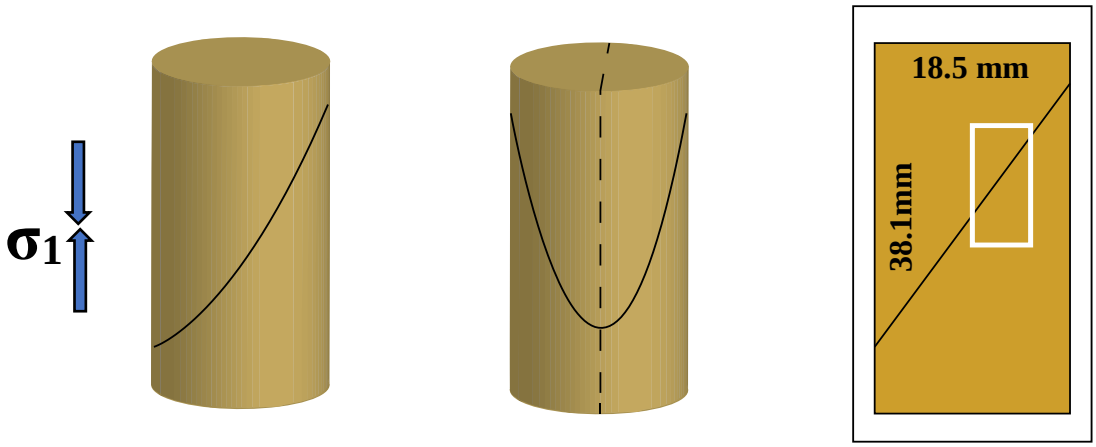

Figure 6: (Left) Illustration of a cylindrical sample with a shear fracture (solid line). (Middle) Shows where the axial cut was made with respect to the fault to create the thin sections (dotted line). (Right) Illustration of a thin section with a white box highlighting the location where photos where taken from samples JU12 and JU7 for the purposes of crack counting and creating the damage maps.

By using a uniformly spaced grid of lines on each photograph, the number of cracks encountered by each transect was recorded. All images taken in this study have an original width of 2.7 mm (representing 2560 pixels in the default photo resolution) and an original height of 2.025 mm (1920 pixels) (see Appendix A4). The spacing used between the grid lines was 275 pixels wide, which corresponds to the

determined mean intercept length of 0.29 mm. This crack counting process was used to determine the crack densities both perpendicular and parallel to the maximum principal stress (Figure 7). For both samples, 64 separate crack densities were determined from counting along vertical transects (parallel to the maximum principal stress, $\sigma\|$) and 80 densities were determined from counting along horizontal transects (perpendicular to the maximum principal stress, $\sigma\perp$).

Additional photographs under the same conditions were taken, and a partial photomosaic of the thin sections could be created and compared by making a semi-quantitative damage map (outlined in Appendix A3).

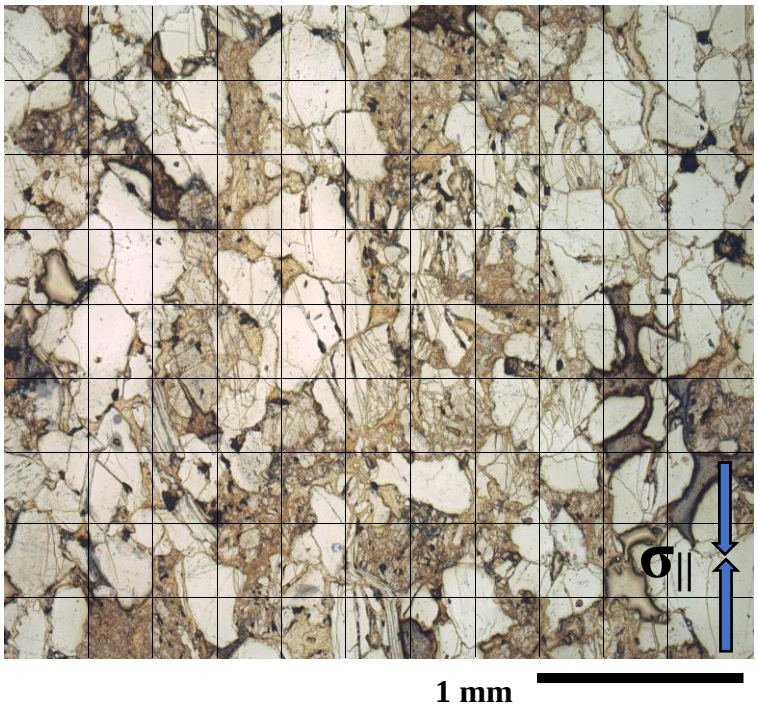

Figure 7 A sample grid that was used to count vertical and horizontal microcrack densities in sample JU7. The image was taken at a total magnification of 50x under normal reflected light. The maximum principal stress was oriented vertically with respect to the image.

2.6: Slip-weakening model

A slip weakening approach was used to analyze the post-peak behavior of each experiment performed in this study (i.e. Rice, 1980). The goal of this model is to quantify the shear stress drop and relative slip weakening distance along a given fault plane. Each of these parameters can be inferred from the experimental data.

The slip weakening model assumes that slip occurs when a fault has fully formed within the sample along one plane oriented at a certain angle (θ) to the maximum principal stress (σ_1). The slip on this surface begins at a peak value of shear stress (τ) and weakens over some critical distance until the fault is assumed to be sliding at its residual strength. To determine the shear stress, drop and slip weakening distance along a given plane within the sample, one must calculate inelastic axial strain (ε_p) by subtracting the elastic strain (ε_{el}) from the total strain (ε_{tot}). The elastic axial strain can be found using the differential stress and measured Young's Modulus (E) (see Figure 6). The axial displacement of the sample can be determined by multiplying inelastic strain by the sample length (L). Given the axial displacement (u_a), the relative slip (u) on any fault plane can be found (Figure 8).

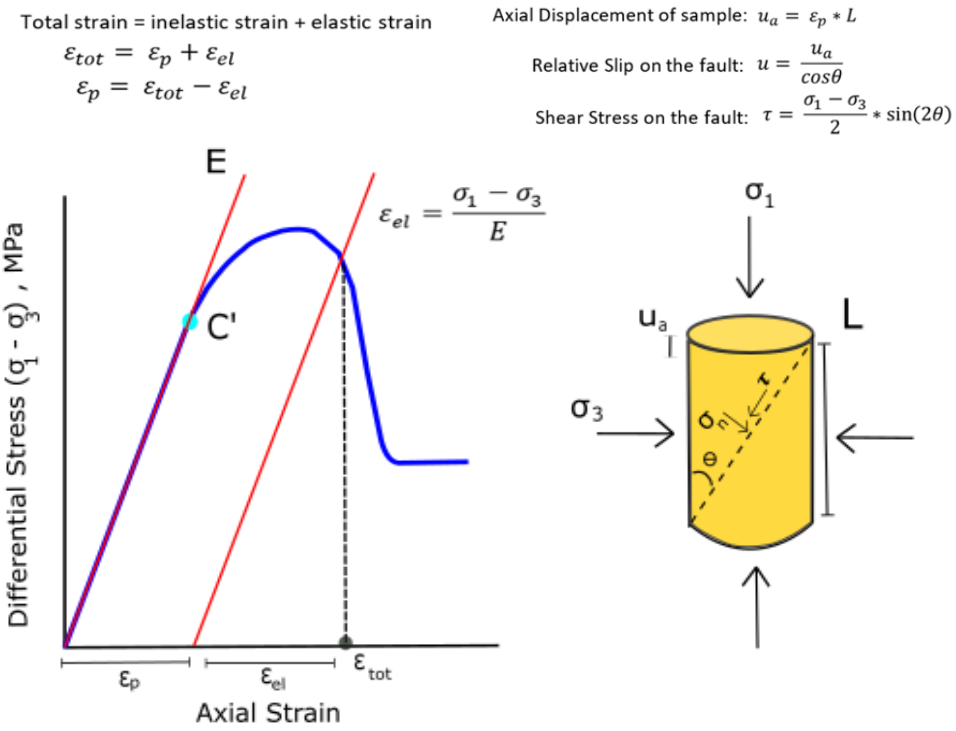

Figure 8: A graphical summary that displays how to calculate shear stress and relative displacement on a fault surface assuming a slip-weakening model

Chapter 3: Results

3.1: Mechanical Data

A series of constant strain rate experiments were performed on fluid-saturated Darley Dale Sandstone, and three different strain rates were investigated: 10^{-4} s^{-1}, 10^{-5} s^{-1}, and 10^{-6} s^{-1}. Every experiment was conducted at an effective pressure of 10 MPa. In the figure and table below, the sample IDs from Table 2 were used except the sample ID was appended to the confining pressure for which the experiment was completed (i.e. JU12-190). The complete set of data are presented in Appendix A1 and A2. There are natural variations between samples taken from different blocks.

The discussion about effects of strain rates and pore fluid pressure on faulting is restricted to samples from the same block with comparable mechanical behaviors.

In the mechanical data presented in Figure 9 and Table 3, compressive stresses and strains were taken to be positive. The volumetric strain (ϵ_v) was calculated following Brace et al. (1966) where the volumetric strain is equal to the axial strain inferred from the axial strain gauge (ε_{ax}) plus two times the radial strain (ε_θ) that was inferred from the horizontal strain gauge (i.e. $\epsilon_v = \varepsilon_{ax} + 2\varepsilon_\theta$). Negative values of volumetric strain denote dilation and positive values indicate compaction. The axial strain in the conventional stress strain curves in Figure 8 were inferred from the axial displacement, as measured from the LVDT on the ram of the hot press. The differential stress represents the difference between the maximum and minimum principal stresses (σ_1-σ_3).

In all experiments, the differential stress-strain curve exhibited an initially short, non-linear progression accompanied by sample compaction as shown by the initially positive volumetric strain values at low differential stress (Figure 9, Left from 0-0.2 % axial strain); this period of deformation is typically interpreted as initial crack closure (Walsh, 1965; Paterson and Wong, 2005). After the initial non-linear period of crack closure, both the volumetric strain curves and differential stress-strain curves proceed in a linear fashion as stress increases; this period of deformation is interpreted to be quasi-elastic (Figure 9, Left from 0.2-0.6 % axial strain; Paterson and Wong, 2005).

After an initial linear increase in both differential stress versus strain and differential stress and volumetric strain, the sample deviates from the previously

described linear behavior. After the sample is elastically loaded, the sample reaches its yield point, and at this point, the sample dilates (increases in volume) as shown by the negative turn in the volumetric strain data (Figure 8). The point at which the volumetric strain data deviates from the initial linear elastic loading and compaction is commonly known as C' or the onset of yielding (Brace et al., 1966; Table 4). After the onset of yielding, rocks deforming in the brittle field are known to dilate due to tensile microcracks opening perpendicular to the maximum principal stress before reaching peak strength (Brace et al., 1966). Rocks deforming brittlely can form a localized shear fracture (Paterson and Wong, 2005). The growth of microcracks after the onset of yielding forms a growing, localized zone of nucleating cracks that eventually fail by shear at the sample's peak strength and result in a stress drop (Reches and Lockner, 1994).

The differential stress-strain data indicate the samples reach peak strength and then subsequently weaken as shown by the negative slope of the stress-strain curve after the sample reaches peak differential stress. Each sample in this study experienced various rates of strain weakening after reaching peak strength (Figure 9), and all samples deformed in this study were found to have formed a localized shear fracture ~30 degrees from the maximum compressive stress (σ_1). For a given strain rate, samples generally show a similar peak strength (within 15 MPa). The effective stress law is likely valid in describing deformation for these experiments since the samples' peak strengths do not systematically vary as a function of pore fluid pressure, and some samples deformed at low versus high pore fluid pressures show nearly identical peak strength (i.e. experiments D21-20 and JU6-130).

Samples deformed at the slow strain rate (10^{-6} s^{-1}) show a spectrum of weakening behavior. Experiment JU7-12 exhibited an abrupt stress drop while all other samples showed varying degrees of slower, more stable weakening. Experiment JU12-190 resulted in the highest residual strength and had the highest peak strength.

Samples deformed at the intermediate strain rate (10^{-5} s^{-1}) showed more consistent weakening behavior than those deformed at 10^{-6} s^{-1}. There is some variation in the peak strength of the samples. Experiment JU11-190 shows a slightly higher peak strength than the others. It also resulted in the smallest stress drop and highest residual strength.

Samples deformed at the fast strain rate showed similar behavior and seem to be the most reproduceable series of samples. Very little difference exists between the low and high pore fluid pressure case at this strain rate. Notably, there is a systematic increase in the peak strength in the fast-strain-rate experiments relative to all other experiments (see appendix A1 and A2; Table 3).

The samples deformed at 190 MPa are likely stronger since P_c may have reached ~193 MPa by the end of these experiments. In order to avoid leaks, the pressure vessel was isloated from the confining pressure intensifier. Because the pressure vessel was isolated, the advancing piston slowly increased the confining pressure throughout deformation. An increase in confining pressure most likely accounts for the systematic increase in strength at P_f = 180 MPa.

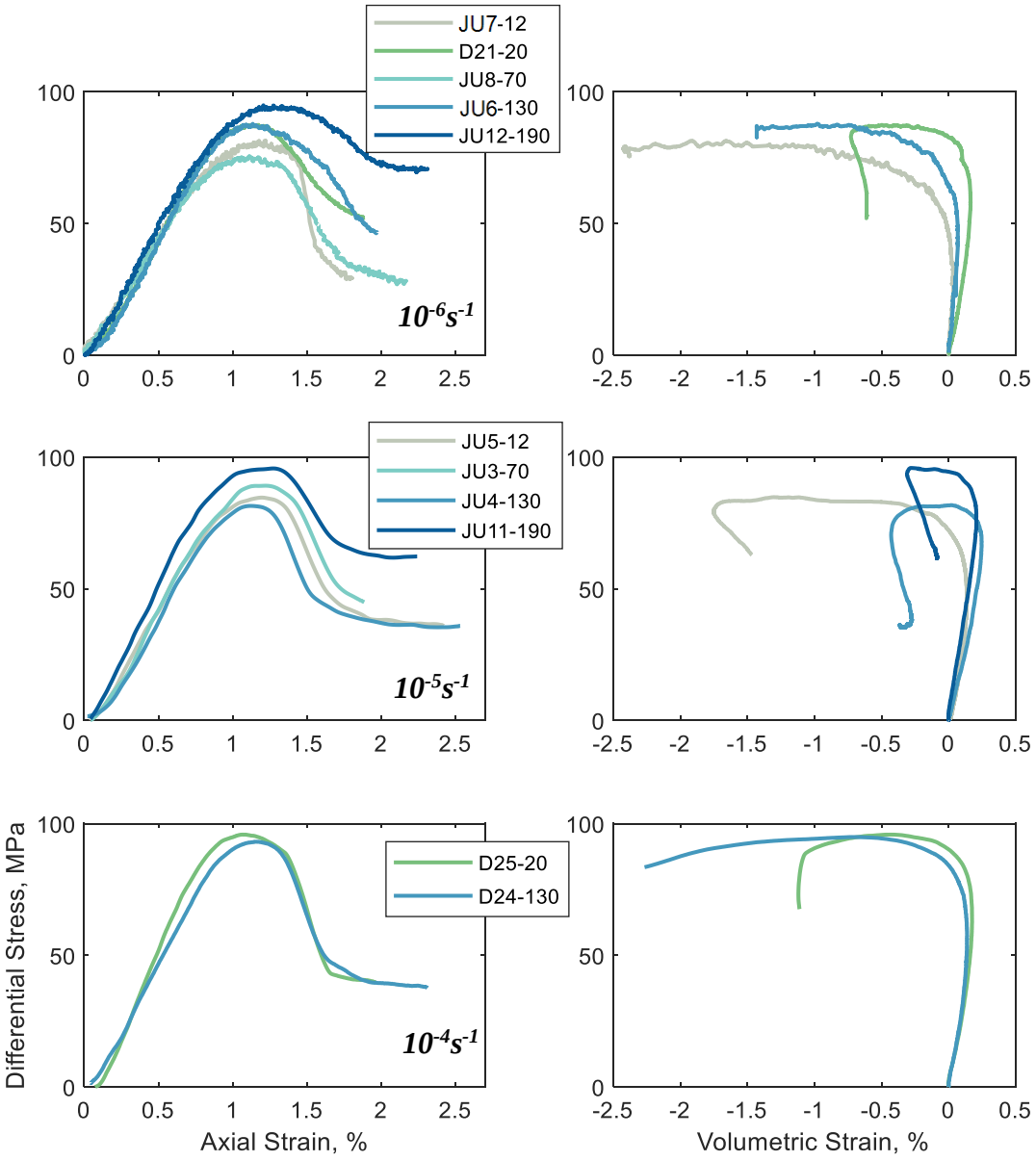

Figure 9: (Left) Stress-Strain curves with axial strain measured from the LVDT on the hot press plotted against the differential stress calculated measured from the force gauge. Each color represents a different confining pressure. All experiments were conducted at an effective pressure of 10 MPa. (Right) Volumetric strain data measured with strain gauges plotted against differential stress. Only experiments with complete strain gauge data are plotted (as outlined in Table 2).

Table 3: Tabulated Data for experiments shown in the main body of the results section. The Poisson's ratio and bulk modulus are inferred from the volumetric strain data.

Sample Code	Strain Rate, s^{-1}	P_c, MPa	P_f, MPa	Peak Strength, MPa	Young's Modulus (E), GPa	Poisson's Ratio (v)	Bulk Modulus (K), GPa
JU7-12	10^{-6}	12	2	81	9.2	-0.35	19.1
D21-20	10^{-6}	20	10	86.5	10.2	-0.23	10.4
JU8-70	10^{-6}	70	60	75	9.3	-	-
JU6-130	10^{-6}	130	120	86	10.2	-0.36	17.7
JU12-190	10^{-6}	190	180	93	10.5	-	13.1
JU5-12	10^{-5}	12	2	85	10.2	-0.21	8.7
JU3-70	10^{-5}	70	60	89	11.4	-	-
JU4-130	10^{-5}	130	120	81	10.6	-0.15	8.1
JU11-190	10^{-5}	190	180	95	11.1	-0.18	10.8
D25-20	10^{-4}	20	10	95	15.7	-0.23	9.5
D24-130	10^{-4}	130	120	94	16.2	-0.28	10.3

3.2: Microstructural Data

Quantitative microstructural analyses were conducted on two end-member samples: JU12-190 and JU7-12. Photomosaics of representative areas of both samples are shown in Figure 10. A damage map was created from representative portions of both samples (further details available in Appendix A3; Figure 6). The damage maps highlight both highly cracked grains with 4 or more *intra*granular cracks that have completely cut across the grain and what was interpreted to be fault debris that consists of very finely crushed material (Figure 9; see Appendix A3 for imaged fault debris). The distributions of observed crack densities from the chord length analysis are shown in Figures 10 and 11. The images for this analysis are made available in Appendix A4. Sample JU12-190 resulted in a microstructure with higher average crack densities oriented parallel and perpendicular to the maximum principal stress direction than sample JU7-12 (Figure 13).

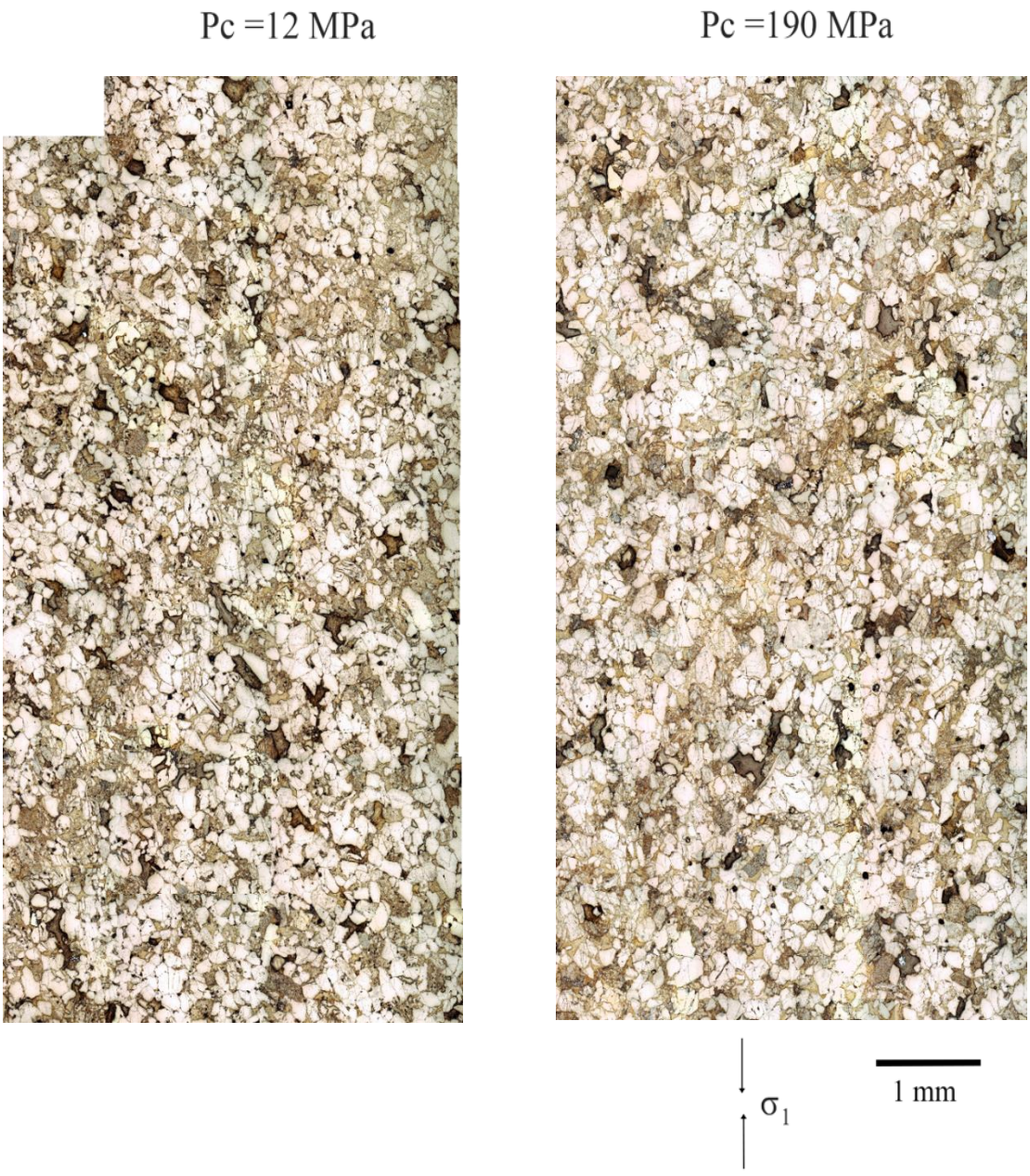

Figure 10: The original photomosaics used to create a semi-quantitative damage map. These photos were taken under a total magnification of 50x under reflected light on a petrographic microscope.

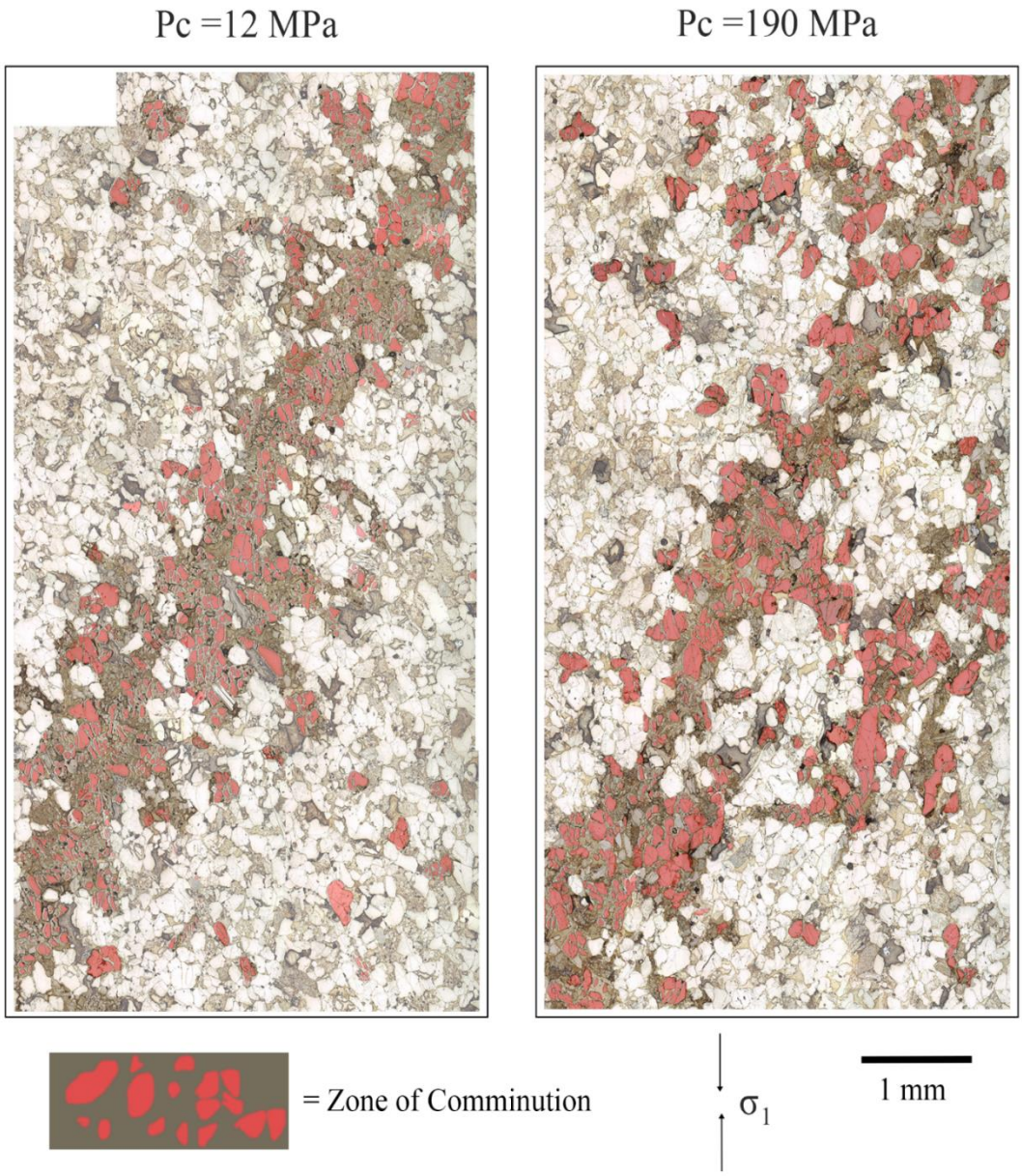

Figure 11: Damage map produced from micrographs of JU12-190 and JU7-12. Zones highlighted brown represent fault debris. Red grains represent grains with 4 or more intragranular cracks. Zones were only highlighted brown if there was both discernable debris and crushed grains that were cognizable.

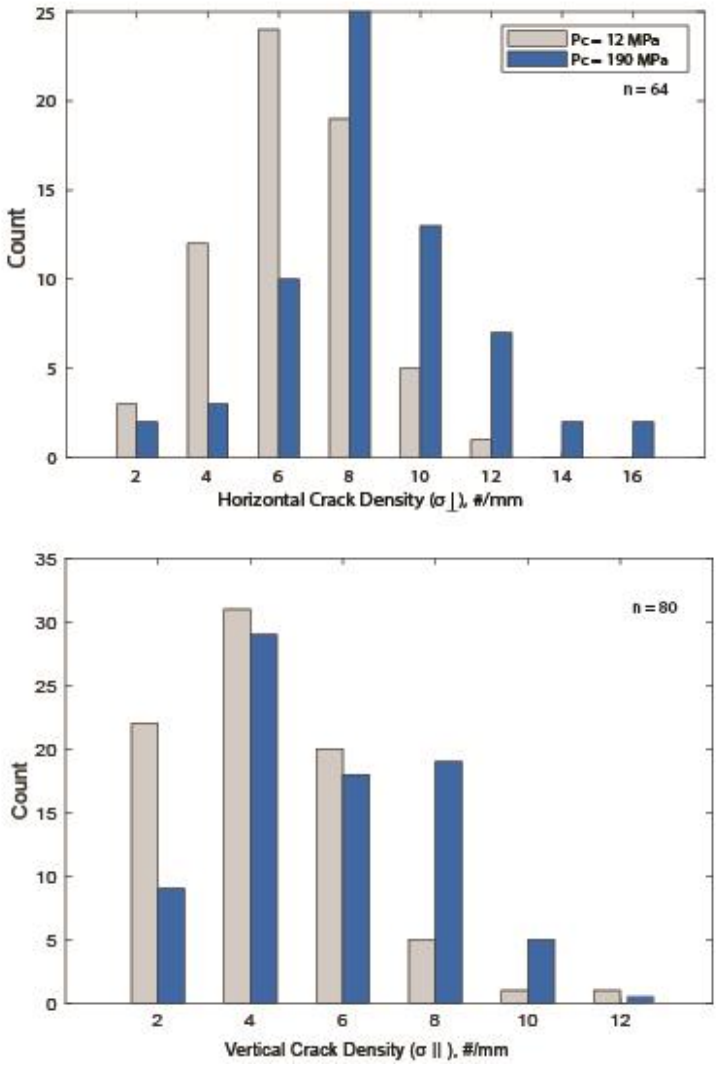

Figure 12: (Top) A histogram showing the crack densities counted perpendicular to the maximum principal stress for samples JU12-190 and JU7-12. The bin centers are shown on the x-axis, and the bins are one unit wide on either side. (Bottom) Displays crack densities counted parallel to the maximum principal stress.

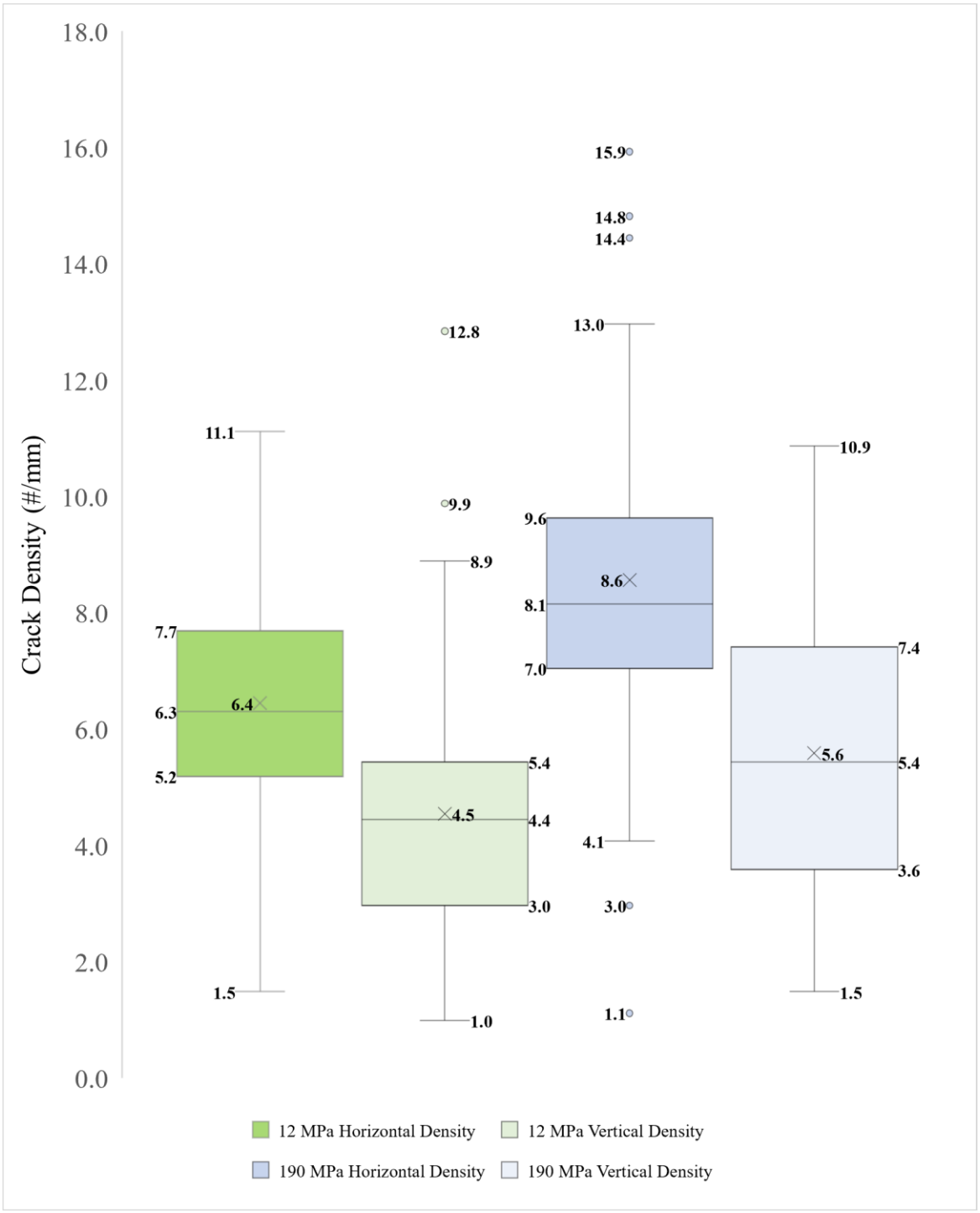

Figure 13: Box-and-whisker plot with data labels that show the upper limit, lower limit, 75th, 50th, and 25th percentiles. The 'X' represents the arithmetic mean of the distributions shown in Figure 10.

Chapter 4: Discussion and Conclusion

4.1: Effect of Pore Fluid and Strain Rate Pressure on Slip Behavior

In order to analyze the weakening behavior of each sample, it is useful to adopt a slip weakening model (outlined in the methodology). For a constant effective pressure of 10 MPa, both the strain rate and value of pore fluid pressure had an important influence on weakening behavior. For instance, increasing the pore fluid pressure led to a smaller stress drop in the case of experiments completed at strain rates of $10^{-6}s^{-1}$ and $10^{-5}s^{-1}$: both experiments JU12-190 and JU11-190 resulted in higher residual strength than all other experiments (Figure 9; Figure 14). The weakening behavior across all experiments is also highly rate dependent. Irrespective of the style of failure that occurred during each experiment, the samples deformed at slow strain rates weakened over a longer timescale. For instance, the samples deformed at the slow strain rate required >1000 s to approach their residual strength. In contrast, the samples deformed at the fast strain rate required ~200 s to reach their residual strength (Figure 14).

Slip-velocity, which can be used to quantify the stability of slip, also depended on the value of pore fluid pressure and the strain rate. A slower loading rate resulted in slower slip velocities and increasing pore fluid pressure resulted in slower behavior in the slow and intermediate strain rate experiments (Figure 15). In the slow series of experiments, the changes in slip velocity in experiments completed with $P_f >$ 2 MPa were subtle and could not be detected with the equipment used to measure axial displacement on the hot press. The observed slip velocities suggest that the

transition to slow-slip behavior occurs at a lower value of pore fluid pressure in the slow experiments than in the intermediate strain rate experiments. In Westerly Granite deformed under drained conditions, the transition from stable to dynamic faulting occurred at lower values of pore fluid pressure when experiments were completed at slower strain rates (see Martin, 1980). The transition between slow and fast faulting in the slow strain rate experiments presented may occur as low as ~10 MPa since the only experiment with considerably fast slip velocity was performed at P_f = 2 MPa (Figure 15). A slower slip velocity was detected at P_f = 180 MPa in the intermediate strain rate series, which suggests that pore fluid pressure must be higher at faster strain rates in order to observe a stabilizing effect (Figure 14).

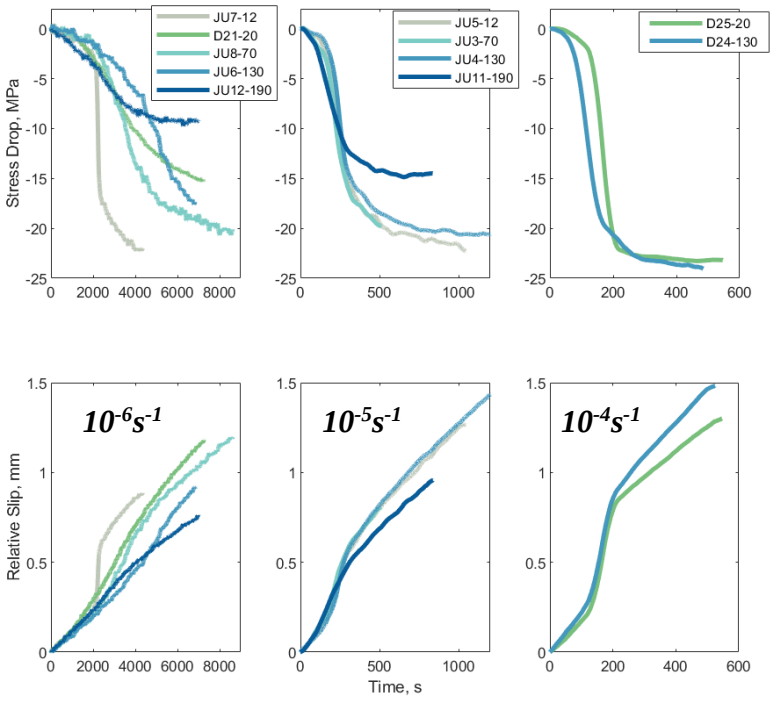

Figure 14: (Top) Shows the shear stress drop versus time along a ~30-degree fault relative to the maximum principal stress. (Bottom) displays relative slip on the fault versus time.

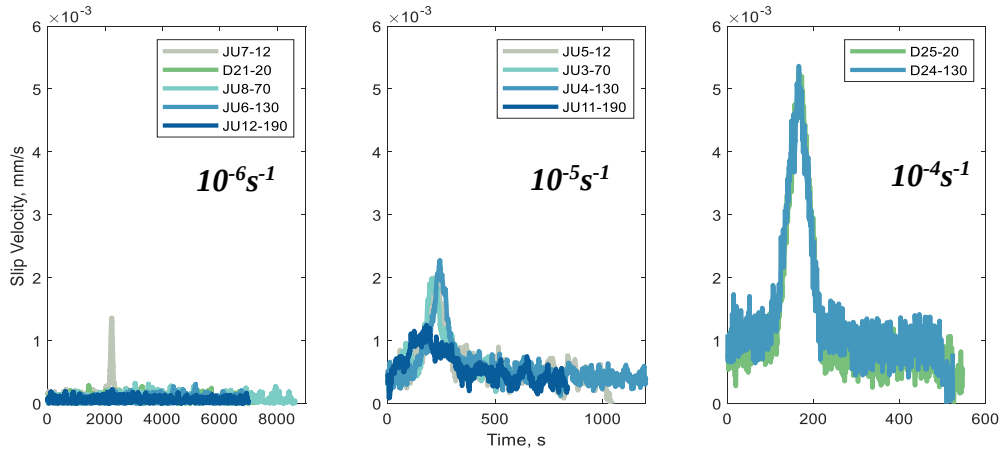

Figure 15: Displays slip velocity (calculated from Figure 13 Bottom). The slip velocity is the time derivative of the relative slip versus time data

4.2 Diffusion Timescale in Porous Rocks

For the experiments conducted in this study, a diffusion timescale can be estimated after Fischer and Paterson (1992) as follows:

$$t = L^2 * \eta * \frac{S}{k}$$

In the case of the experiments conducted in this study, the diffusion time (t) can be estimated as t = 0.025 s given a sample length (L) of 0.05 m, viscosity of water (η) equal to 10^{-3} Pa*s, storage capacity per unit volume (S) of 10^{-10} Pa^{-1}, and permeability (k) of 10^{-14} m^2 (see Zhu and Wong, 1997). Duda and Renner (2013) measure the storage capacity per unit volume of certain sandstones and report values between ~10^{-10} and 10^{-11} Pa^{-1}. At an effective pressure of 10 MPa, Zhu and Wong (1997) measured the permeability of Darley Dale sandstone and report values of ~10^{-14} m^2. The diffusion time (t) is likely less than or equal to 1 second even if values of S or k vary an order of magnitude. Consequently, for all experiments shown in this study, it is valid to assume most of the deformation is well-drained since t is much

less than the total time it takes for a sample to be deformed, which varies between ~5 minutes for samples deformed at 10^{-4} s^{-1} and up to ~7 hours for samples deformed at 10^{-6} s^{-1}. Therefore, one may not expect significant dilatant hardening to occur in a high-permeability, porous rock such as Darley Dale sandstone, if the bulk permeability of the sample is the primary variable that determines the occurrence of dilatant hardening.

Although the bulk of the sample is drained over the timescale of a whole experiment, drainage may not be maintained on a local scale during the microscale precursory damage (i.e. Renard, 2017) that occurs prior to faulting. Notably, porous and crystalline rocks have fundamentally different rupture nucleation processes and permeability evolution prior to failure. For porous rocks in the brittle regime, permeability has been shown to decrease after the onset of shear enhanced dilatancy (C'), but in crystalline rocks, permeability has been shown to increase after the onset of dilatancy (Zhu and Wong, 1997).

In porous rocks, damage prior to faulting is accompanied by both compaction (pore collapse) and dilatant damage (primarily tensile microcracking), but in crystalline rocks, deformation is strictly dilatant (Renard et al., 2017). From a theoretical standpoint, the model formulated by Rudnicki and Chen (1988) assumes that the stabilization of failure is governed by the drainage condition at a frictionally sliding fault that has completely formed within a sample. However, the microstructural observations by French and Zhu (2017) suggest that dilatant hardening has an integrated effect that occurs on many nucleating cracks throughout the sample. This indicates dilatant hardening could occur in porous rock if there are

local decreases in permeability that are drastic enough to inhibit drainage at the grain scale. In porous rock, a negative correlation exists between porosity and permeability; when total pore volume increases after brittle faulting, bulk permeability has been observed to decrease roughly one order of magnitude due to the formation of an impermeable shear band that contains highly crushed grains (Zhu and Wong, 1997; Menéndez et al., 1996). Therefore, it is reasonable to believe that porous rocks may experience significant local variations in permeability as fractures begin to cluster and the rock approaches peak strength during deformation. These local permeability variations in highly damaged areas could lead to dilatant hardening and distributed deformation.

4.3: Dilatancy and Slip-Behavior

In order to describe the ratio between an increment of dilation and plastic shear strain, Rice (1975) introduced the dilatancy factor β. The dilatancy factor may be calculated using inelastic axial strain and inelastic volumetric strain as follows (see Wong et al., 1997):

$$\beta = -\sqrt{3}\frac{\Delta\varepsilon_{v,p}/\Delta\varepsilon_p}{3 - \Delta\varepsilon_{v,p}/\Delta\varepsilon_p}$$

$\Delta\varepsilon_p$ represents an increment of inelastic axial strain (see Figure 8). In the above equation, $\Delta\varepsilon_{v,p}$ represents an increment of inelastic volumetric strain, which is calculated by subtracting the elastic component of volumetric strain from the total amount of volumetric strain:

$$\varepsilon_{v,p} = \varepsilon_{tot,v} - \frac{\sigma_{effm}}{K}$$

$\varepsilon_{tot,v}$ represents the total amount of volumetric strain, K is the bulk modulus, and σ_{effm} is the effective mean stress (Table 3). In order to calculate the dilatancy factor (β), the maximum change in $\Delta\varepsilon_{v,p}/\Delta\varepsilon_p$ was estimated from a graph of the inelastic volumetric strain and inelastic axial strain (Figure 16). The maximum change in $\Delta\varepsilon_{v,p}/\Delta\varepsilon_p$ occurred slightly prior to the peak strength of the sample. Samples deformed at the intermediates strain rate resulted in the lowest β values while samples deformed at the fast and slow strain rates resulted in higher β values (Figure 16).

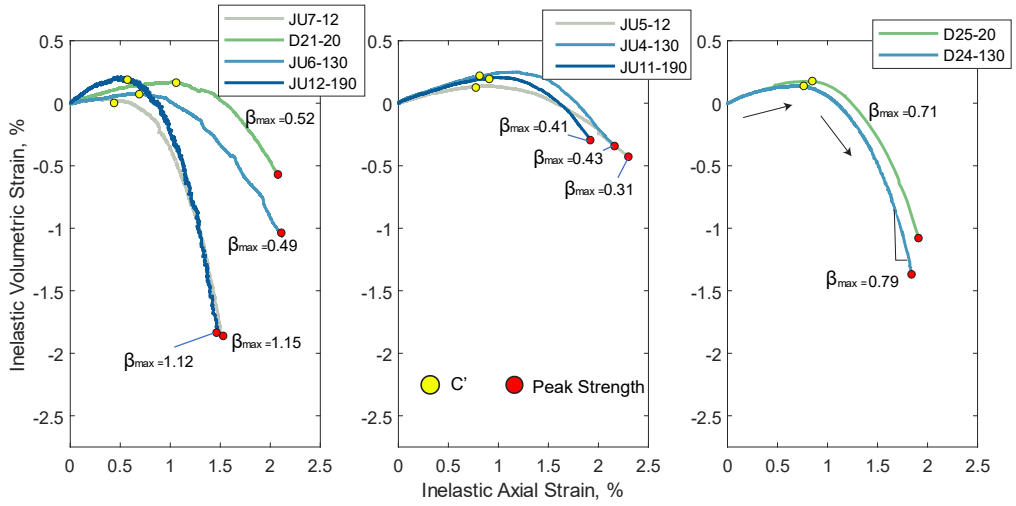

Figure 16: Shows inelastic volumetric strain plotted against inelastic axial strain (described in text). The black arrows are included to demonstrate that the sample was loaded from 0% inelastic strain until failure. The bulk moduli and Young's moduli used to calculate these curves are given in Appendix A1 and Table 3. The maximum β value was calculated by estimating the slope of the steepest portion of each curve (black slope line). The yellow dot denotes the onset of yielding (C') and the red dot marks when the sample reaches peak strength during the deformation experiment.

Experiments JU7-12 and JU12-190 share nearly the same β value but showed vastly different weakening behavior (Figure 14; Figure 15; Figure 16). If dilatant hardening is to explain stabilized failure behavior, one might expect a higher β value for a higher value of pore fluid pressure at a given strain rate; instead, the slow series

of experiments demonstrates that similar β values can result in vastly different weakening behaviors despite a drastic change in pore fluid pressure. This could indicate that the micromechanical process that caused stable weakening behavior in experiment JU12-190 manifested after the peak strength of the sample was reached. In order to measure any difference in dilatant behavior after the samples reaches peak strength, pore volume change and permeability could be measured after the sample reaches peak strength. In the intermediate strain rate series, each experiment also shared a similar β value. These observations suggest that the stable weakening behavior seen at P_f = 180 MPa cannot be explained by distinct dilatant behavior prior to the sample's peak strength.

Increasing the strain rate to 10^{-4} s^{-1} causes an increase in the β value compared to the intermediate strain rate experiments (Figure 16). This observation aligns well with dilatant hardening as it is described by Brace and Martin (1968). Accordingly, experiments at the fast strain rate resulted in a higher peak strength than those performed at the other strain rates with the same pressure conditions. This indicates that effective drainage may have been lost after the sample yielded because the deformation was too fast to allow for the drainage of pore fluid to newly created void spaces (Duda and Renner, 2013; Brace and Martin, 1968). Despite causing more dilatancy prior to failure, the value of pore fluid pressure at the fast strain rate did not cause a measurable change in slip behavior Figure 14; Figure 15). This suggests that the fast loading rate is likely more influential on the slip behavior than the value of pore fluid pressure. Despite a negligible impact on slip behavior, a higher β value at the fastest loading rate suggests that the undrained deformation could result in distinct

precursory behavior (in the form of enhanced dilatancy) if deformation is sufficiently fast.

4.4 Micromechanical Mechanisms

In addition to the mechanical data, the microstructural observations suggest that the micromechanical processes governing fault growth in experiments JU12-190 and JU7-12 were different. In the high pore fluid pressure case, crack densities were higher in zones around the localized shear band (Figure 13). In addition to localized deformation along a fault oriented ~30 degrees from the maximum principal stress, the high pore fluid pressure experiment resulted in a substantial amount of cataclasis away from what one may interpret to be the main fault (Figure 11). These cracks remain small in comparison to the macroscopic fault plane and never propagated to form an apparent macroscopic feature.

The theory of subcritical crack growth can describe the process responsible for the larger number of small, distributed cracks that occurred in the high pore fluid pressure case (Figure 11). In fracture mechanics, for a crack to propagate unstably, the critical stress intensity factor (K_c) must be exceeded at the crack tip (Figure 17; Atkinson, 1984). However, it is well known that cracks may stably grow when the stress intensity factor is well below K_c (Atkinson, 1984). The theory of subcritical crack growth describes the lengthening of a crack when the stress at the crack tip is below a critical value that is characterized by K_c but above the minimum value K_o which describes the minimum stress intensity at a crack that allows for stable crack growth. Phase 1 of subcritical cracking is controlled by the rate of stress corrosion cracking: a mechanism where strained Si-O bonds in silicate-rich rocks may react

with the interstitial aqueous fluid to form a hydrolyzed Si-OH bond that can be broken at lower stresses than the Si-O bond (Anderson and Grew, 1977; Baud et al., 2000; Atkinson, 1984). Phase 2 is controlled by the rate of diffusion of the pore fluid to the crack tip, and phase 3 represents the unstable rupture of the crack (Atkinson, 1984). The presence of many distributed cracks at Pf = 180 MPa suggests that there is a micromechanical mechanism that increases K_c at crack tips (Figure 17).

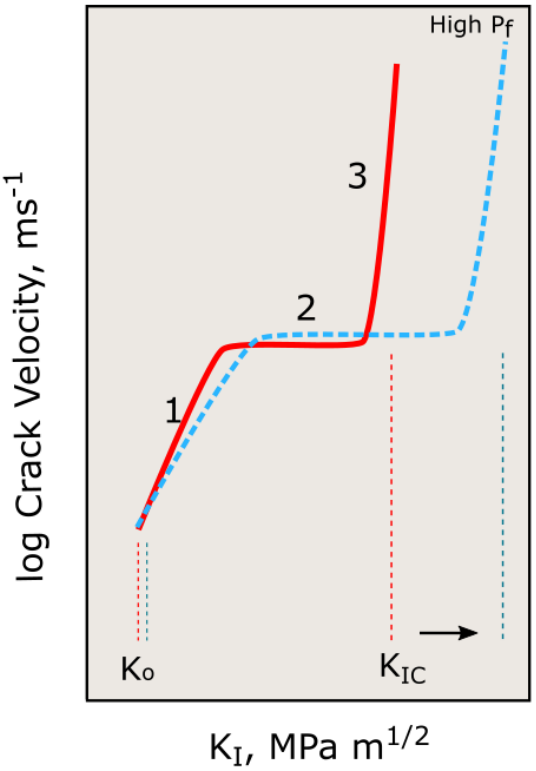

Figure 17: A classical graph of crack velocity plotted against the mode 1 stress intensity factor (K_I) (adopted from Atkinson, 1984). A crack may grow slowly prior to reaching a critical stress (K_c) and propagating unstably (Red cruve; see text for explanation). High pore fluid pressure may increase the critical stress intensity factor and therefore allow for a crack to slowly grow under a higher stress intensity (Blue dashed curve).

As previously mentioned, local variations in permeability may ultimately lead to dilatant hardening and cause slower slip and a smaller stress drops at high pore fluid pressure. The enhanced cracking away from the "fault" that is evident is sample JU12-190 may indicate cracks could not easily link to form a macroscopic fault due

to a clamping effect at crack tips that was caused by an undrained condition and locally high effective normal stress (i.e. French and Zhu, 2017). Within the context of subcritical crack growth, any clamping effect at a crack that is caused by a locally undrained condition would result in two phenomena: (1) K_c will increase because there is higher effective normal stress on the crack tip, and (2) dynamic rupture will be limited by the rate of diffusion to the crack tip (described by phase 2 of subcritical crack growth) because of a local decrease in permeability (Blue dashed curve, Figure 17). Essentially, this is dilatant hardening as it was traditionally described by Rudnicki and Chen (1988) and Rice (1975) but occurring on the length scale of a few microns at microcrack tips.

Grain comminution and the formation of an impermeable shear band is known to cause a decrease in the sample's permeability (Zhu and Wong, 1997). Enhanced cracking and distributed deformation in the high pore fluid pressure case could be indicative that local variations in permeability around the time of localization drastically stabilized weakening behavior and resulted in dilatant hardening. The end-result of this was an anastomosing fault (a broader, highly damaged area) with higher cohesive strength (as seen in the mechanical data). Ultimately, local variations in permeability, and not the bulk permeability of the sample, may have a critical influence on the weakening behavior of the sample. These variations in local permeability may be most important at P_c =190 MPa and P_f = 180 MPa when confinement is the highest. The onset of grain crushing (P^*) for Darley Dale sandstone occurs when the rock is confined at an effective pressure of ~210 MPa (Wong et al., 1997; Wu et al., 2000). Therefore, at a confinement of 190 MPa, the

stress concentration at grain-to-grain contacts may be great enough to result in Hertzian fracture and cataclasis that occurs at a random orientation as opposed to the preferred orientation (~30 degrees from σ_1) as predicted by Mohr-Coulomb theory. However, further experimental work is needed to test this hypothesis.

Chapter 5: Concluding Remarks

Triaxial deformation experiments were performed on water-saturated samples of Darley Dale sandstone while using a constant effective pressure of 10 MPa and pore fluid pressures ranging from 2 to 180 MPa. The mechanical data and microstructural observations demonstrated that the value of pore fluid pressure and the loading rate had an important influence on the failure behavior of porous rock. This work directly complements analogous work completed on Westerly Granite and serpentinite (i.e. French and Zhu, 2017; Martin, 1980). My data show that slip velocity was decreased with decreasing strain rate and increasing pore fluid pressure (Figure 15). Inelastic deformation prior to failure was also rate-dependent; subcritical cracking is the primary mechanism for dilatancy at the slow strain rate, and at the fast strain rate, loss of internal drainage around the peak strength of the sample may have enhanced dilatancy prior to failure.

The microstructural analysis and mechanical data both suggest that the micromechanical mechanisms operating at P_f =180 MPa versus P_f = 2 MPa were different under well-drained conditions at a strain rate of $10^{-6}s^{-1}$. Despite similar inelastic behavior prior to failure, high pore fluid pressure exacerbated grain comminution and thus caused significant local variations in permeability that led to dilatant hardening. At high pore fluid pressure, zones of many small microcracks

never grew large enough to create a more macroscopic shear band; therefore, I infer that these cracks grew subcritically because there were local increases in effective normal stress on crack tips that led to a higher critical stress intensity factor (Figure 17). As previously mentioned, a locally undrained condition will lead to a scenario where fault rupture is controlled by the rate of diffusion to the crack tip. The grain crushing that lead to local changes in permeability at high pore fluid pressure likely occurred when the rock reached peak strength or slightly afterward (Figure 14; Figure 15).

The intermediate series of experiments resulted in the lowest β values, which could be indicative of a drained condition where the timescale does not allow for significant subcritical cracking around the sample's peak strength. Like the slow series, the β value did not vary with pore fluid pressure. The slip velocity data suggest that the transition to more stable behavior occurred at a higher value of pore fluid pressure when the strain rate was increased one order of magnitude (Figure 15). A faster strain rate should lessen subcritical cracking and lead to a more localized fault zone.

Increased pore fluid pressure at the fast strain rate led to distinct precursory behavior that involved more inelastic volumetric strain per increment of inelastic shear strain (higher β value). Although this effect had no measurable effect on the slip behavior, it demonstrates that the deformation rate can lead to an undrained condition and subsequently higher peak strength (i.e. Brace and Martin, 1968; Duda and Renner, 2013).

If dilatant hardening is indeed insensitive to initial porosity and permeability of a rock, then it may be a process that has more applicability to natural faulting than previously thought. Additionally, these data provide more evidence to support the idea that the value of pore fluid pressure can dictate failure behavior; this is an observation beyond what can be predicted with Mohr-Coulomb theory and the effective stress law. In nature, the data presented here have important implications for the mechanical behavior of the up-dip portion of subduction zones where episodic tremor and slow slip activity is commonly observed (Tobin and Saffer, 2009). In this region, pore fluid pressure is commonly inferred to be near-lithostatic and effective pressure is assumed to be low (Tobin and Saffer, 2009; Figure 1). In this portion of the subduction zone, high pore fluid pressure could be the primary factor that causes slow slip behavior. Additionally, the data presented here suggest that high pore fluid pressure may impede rupture on brittle faults and result in slow slip behavior regardless of the initial permeability of the fault zone.

Appendices

A1: Summary of All Experimental Data

A summary of all mechanical data completed for this thesis is presented in the table below.

Pc, MPa	**Pf, MPa**	**Strain Rate, s^{-1}**	**Sample ID**	**Young's Modulus, GPa**	**Bulk Modulus, GPa**	**Poisson's Ratio**	**Aprox. Weakening Duration, s**	**Peak Strength, MPa**	**Thin Section (Y,N)**
12	2	10^{-6}	JU7	9.2	19.1	-0.35	4000	81	Y
20	10	10^{-6}	D21	10.2	10.2	-0.23	7410	86.5	N
20	10	10^{-6}	D22	10.8	8.1	-0.17	1510	89	N
70	60	10^{-6}	JU8	9.3	-	-	7970	75	N
130	120	10^{-6}	JU6	10.3	17.7	-0.37	6880	86	N
130	120	10^{-6}	D20	11.9	10.6	-0.20	1620	91	Y
190	180	10^{-6}	JU12	10.5	-	-	9670	93	Y
12	2	10^{-5}	JU5	10.2	8.7	-0.21	950	85	Y
70	60	10^{-5}	JU3	11.4	-	-	> 492	89	N
130	120	10^{-5}	JU4	10.6	8.1	-0.15	840	81	N
130	120	10^{-5}	D29	13.1	11.3	-0.23	905	93	N
190	180	10^{-5}	JU11	11.1	10.8	-0.18	805	95	Y
20	10	10^{-4}	JU9	10.8	7.4	-0.14	154	91	N
20	10	10^{-4}	D26	15.8	-	-	210	95	N
20	10	10^{-4}	D25	15.7	9.5	-0.23	285	95	N
130	120	10^{-4}	D24	16.2	10.3	-0.28	270	94	N
130	120	10^{-4}	JU10	10.9	8.8	-0.15	338	92	Y

A2: All Mechanical Data

Mechanical Data included in the main text and all other mechanical data not included in the main text.

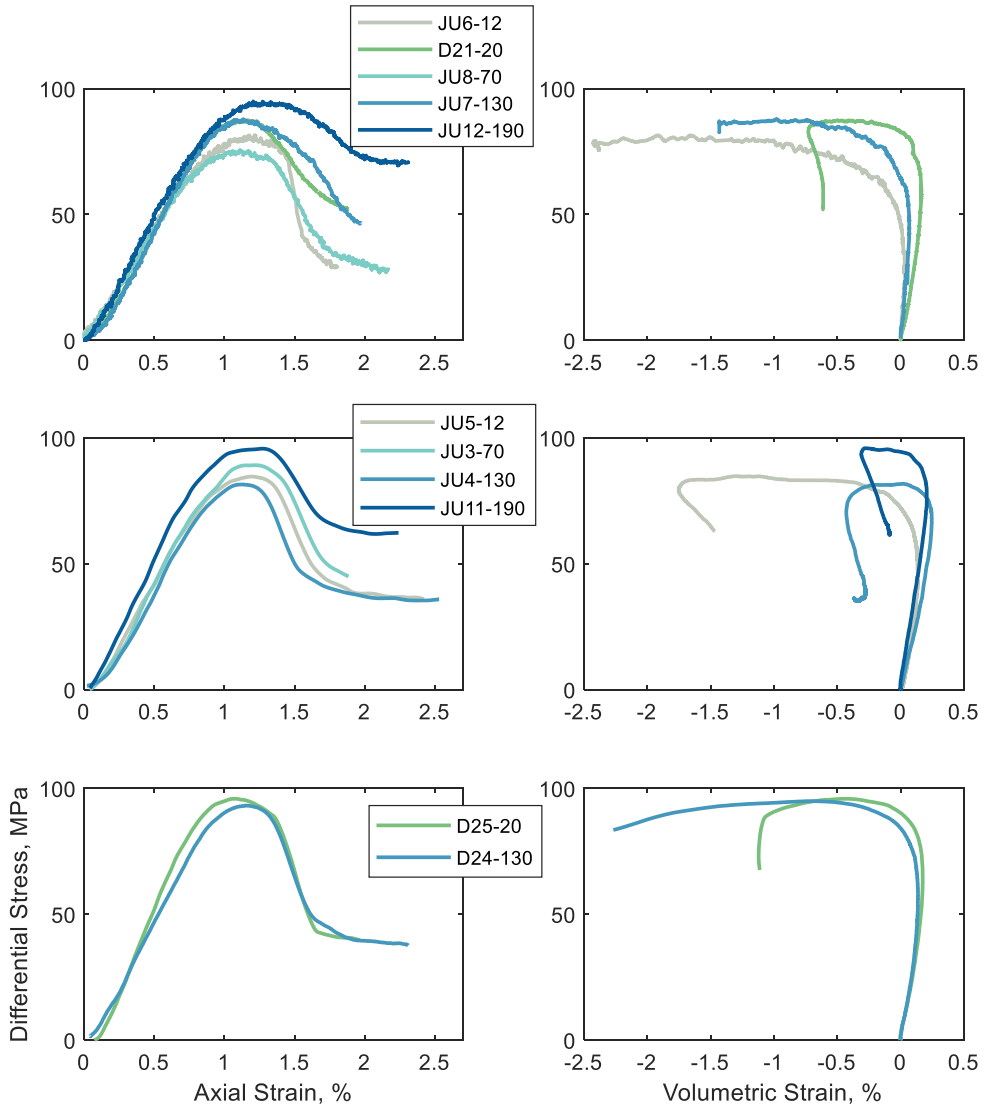

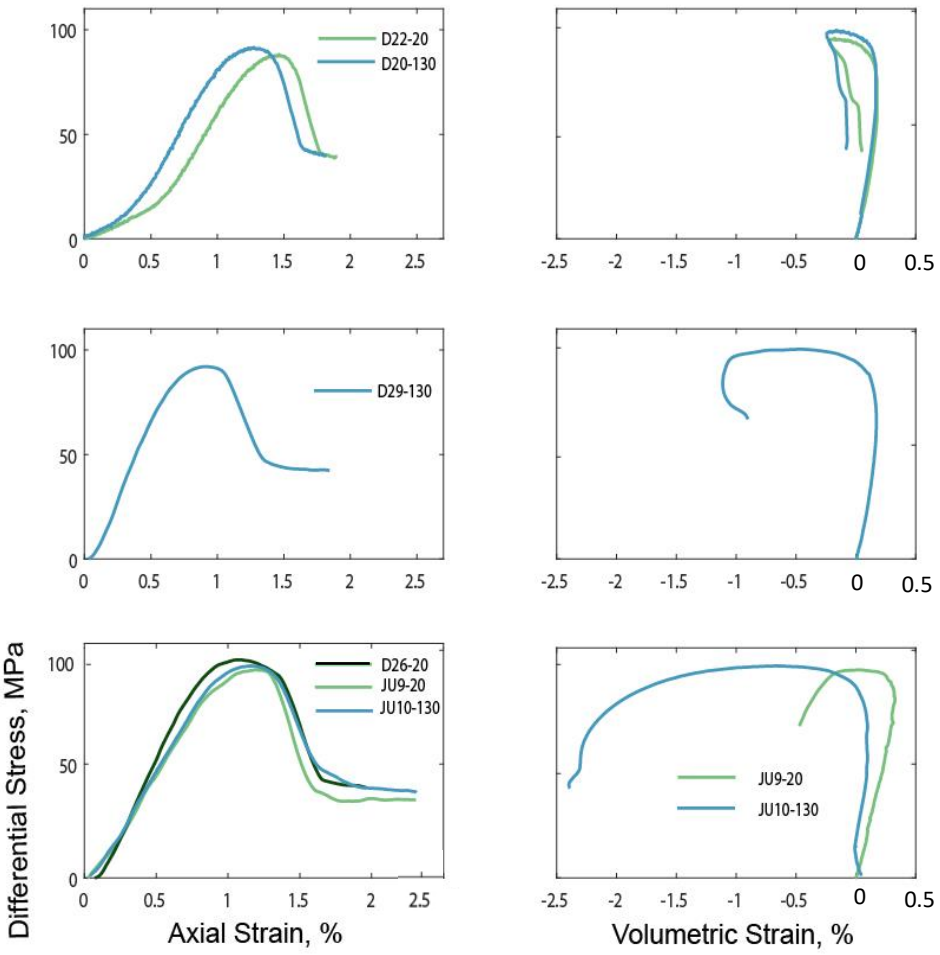
D22-20
D20-130
D29-130
D26-20
JU9-20
JU10-130
Differential Stress, MPa
Axial Strain, %
Volumetric Strain, %

A3: Damage Criterion for Displayed Damage Maps

Shows an example of how damage in thin section was interpreted to create the damage map. Grains were manually filled in with an image tracing technique in Adobe Illustrator. A grain was filled with red around its boundary when at least 4 intragranular cracks could be identified. The damage map is binary, meaning a grain is red or left alone. The top image is uninterpreted from JU7-12. The bottom image shows in-filled red grains with 4 or more intragranular cracks. Images are under 50x magnification and normal reflected light

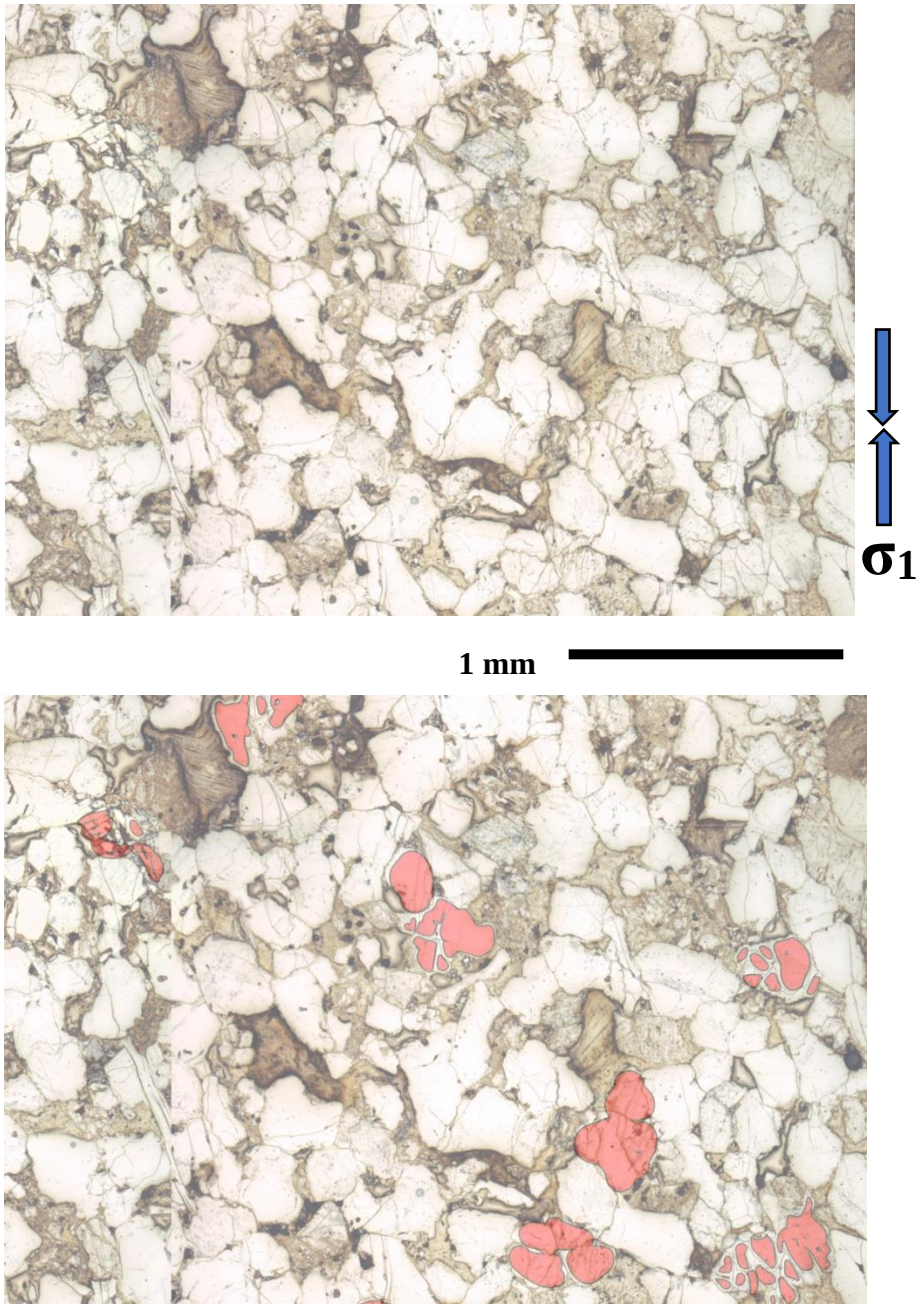

Fault debris is also pervasive throughout both samples. Below is an example from JU12-190. The image is taken under normal reflected light at a total magnification of 100x. In the case where there is fault debris and grains with 4 or more intragranular cracks, the photo what highlighted brown to signify the presence of such debris and represents an area with abundant grain comminution.

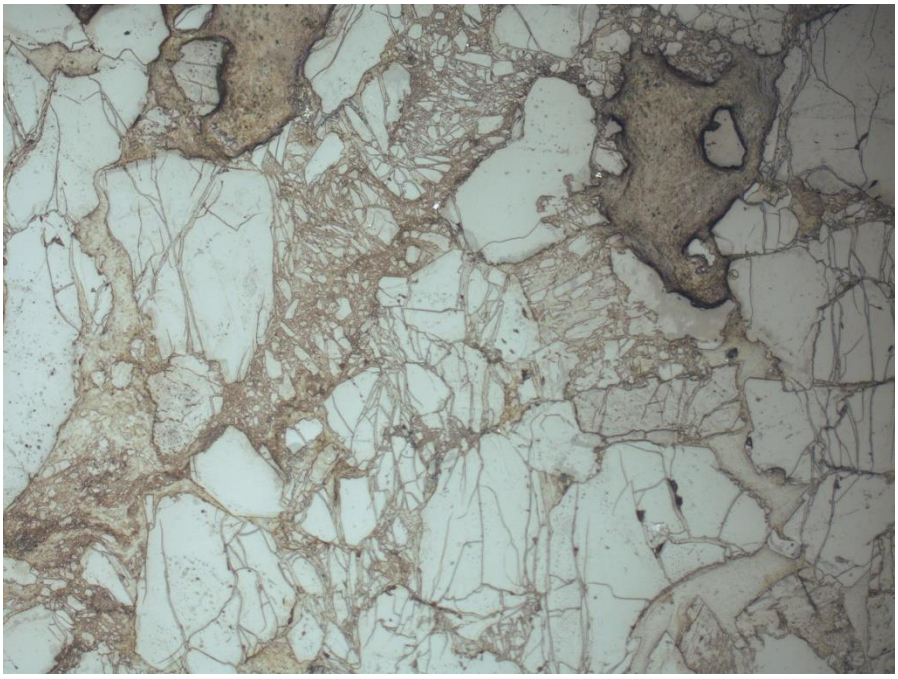

1 mm

Defines what is meant by “4 or more intragranular cracks.” For a grain to be highlighted red, 4 or more cracks must traverse the entirety of the grain.

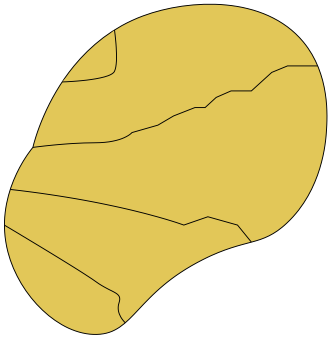

A4: Images used for Chord Length Analysis

On the next page are all the photos used to determine the average crack densities both parallel and perpendicular to the maximum principal stress (as seen in Figures 12 and 13). The grid shown in Figure 7 was used to count cracks. First, photos from JU12-190 are shown. Then, photos from JU7-12 are shown.

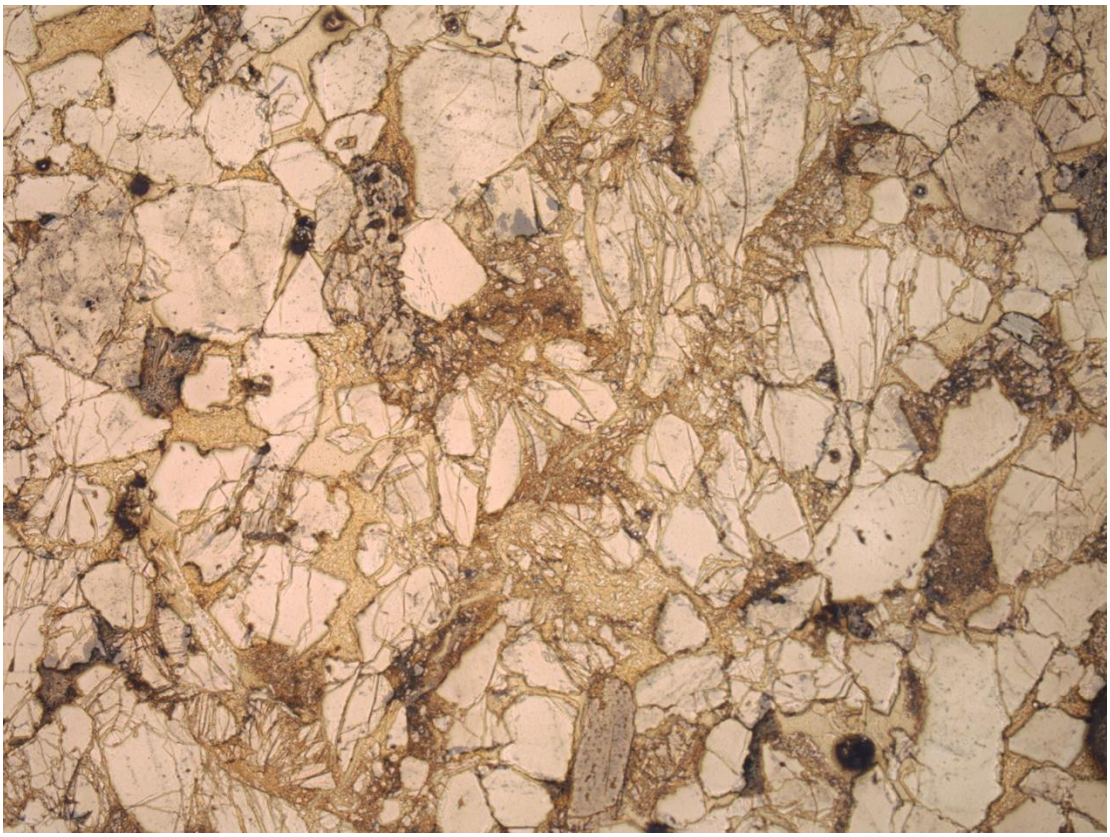

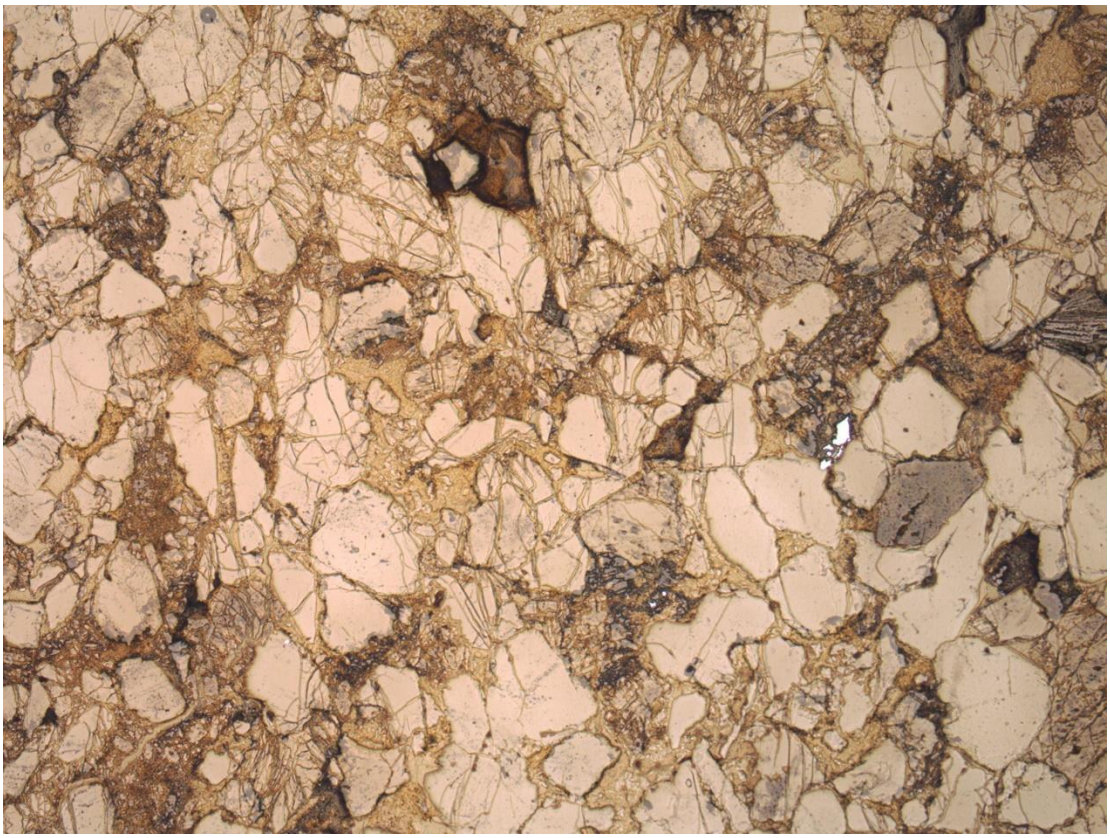

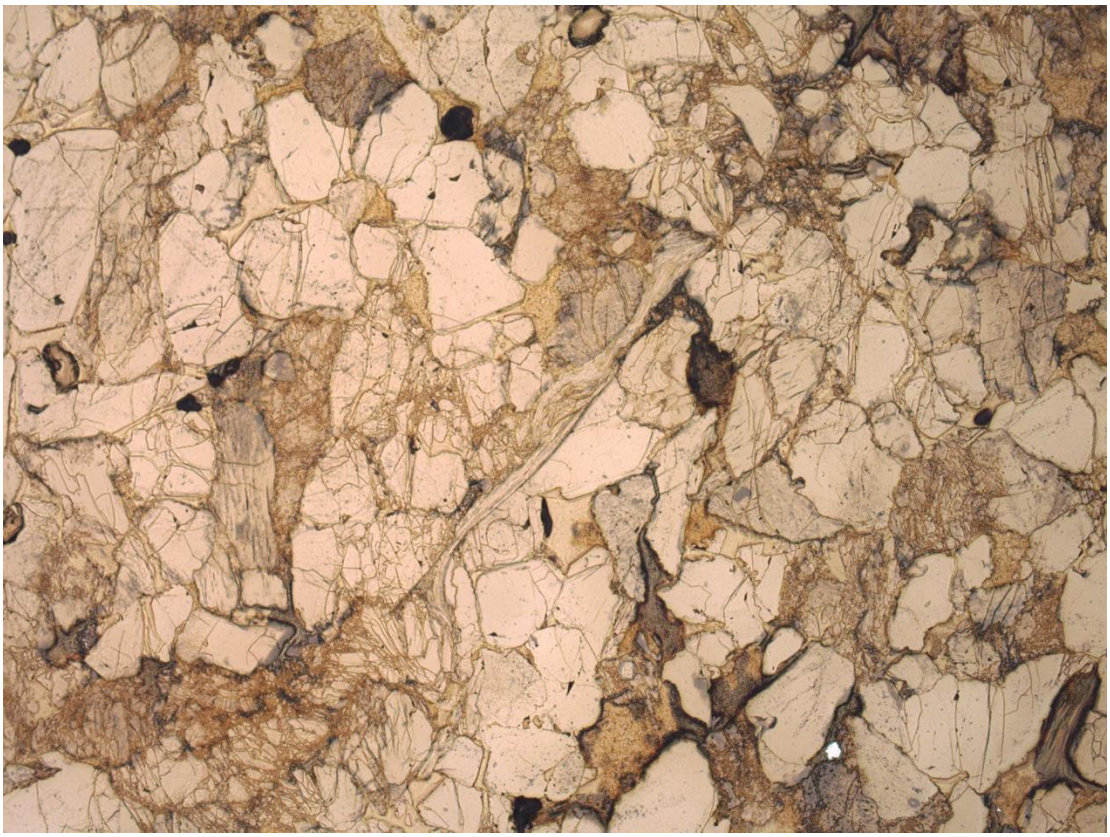

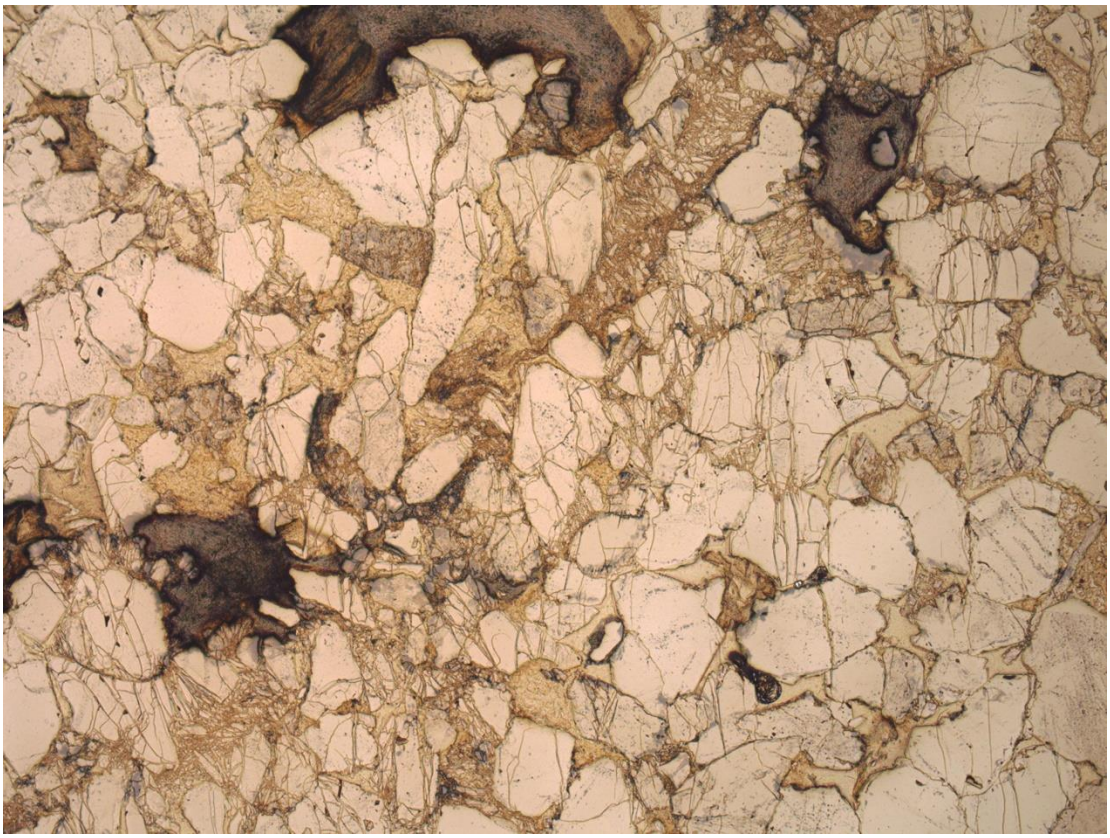

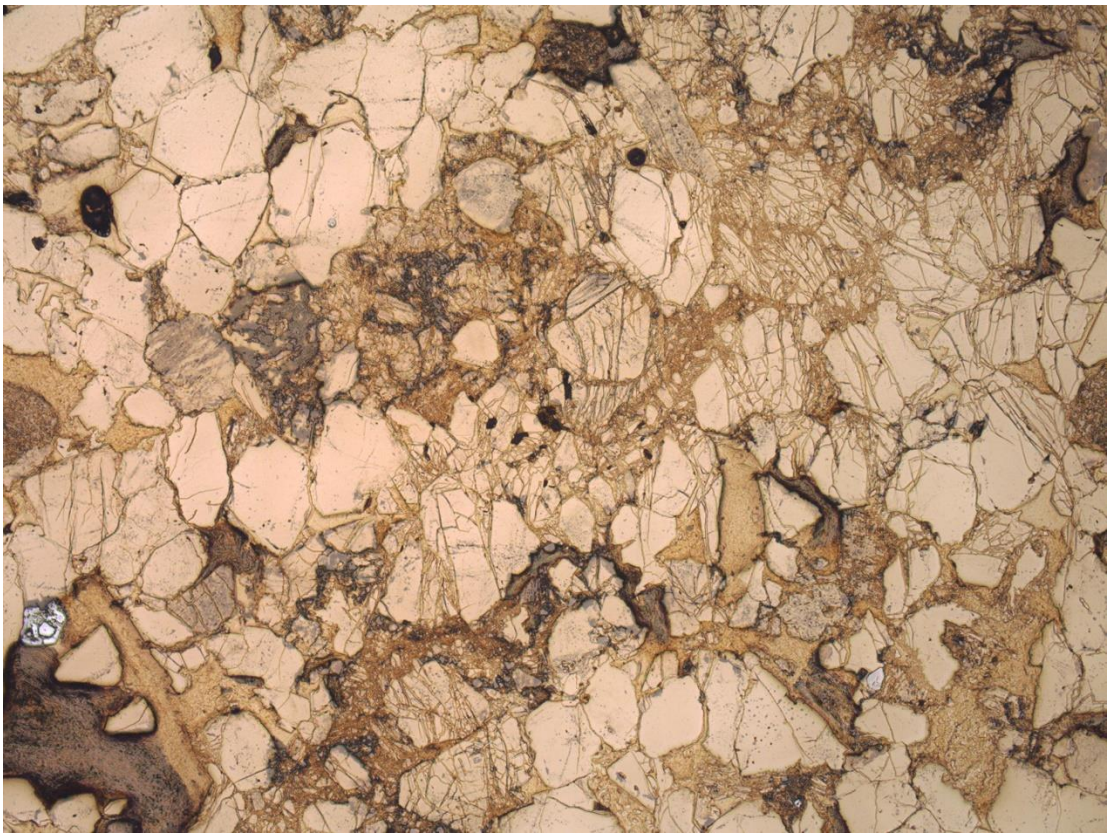

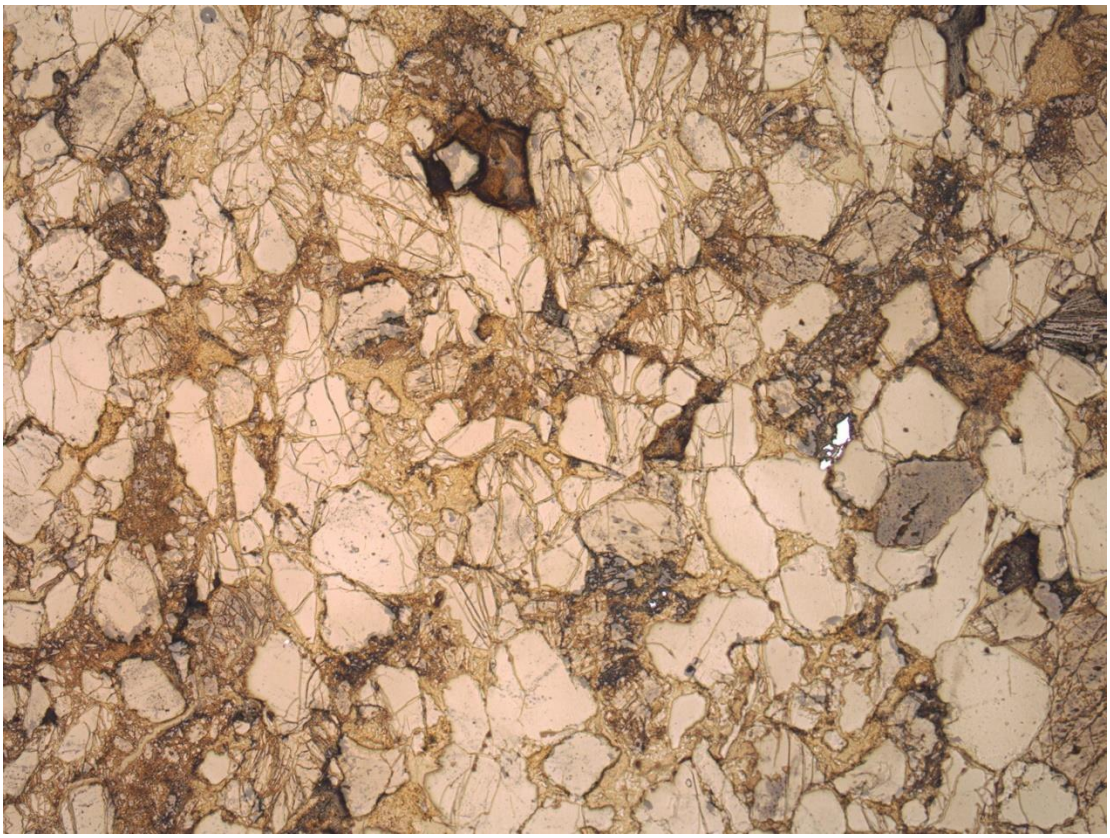

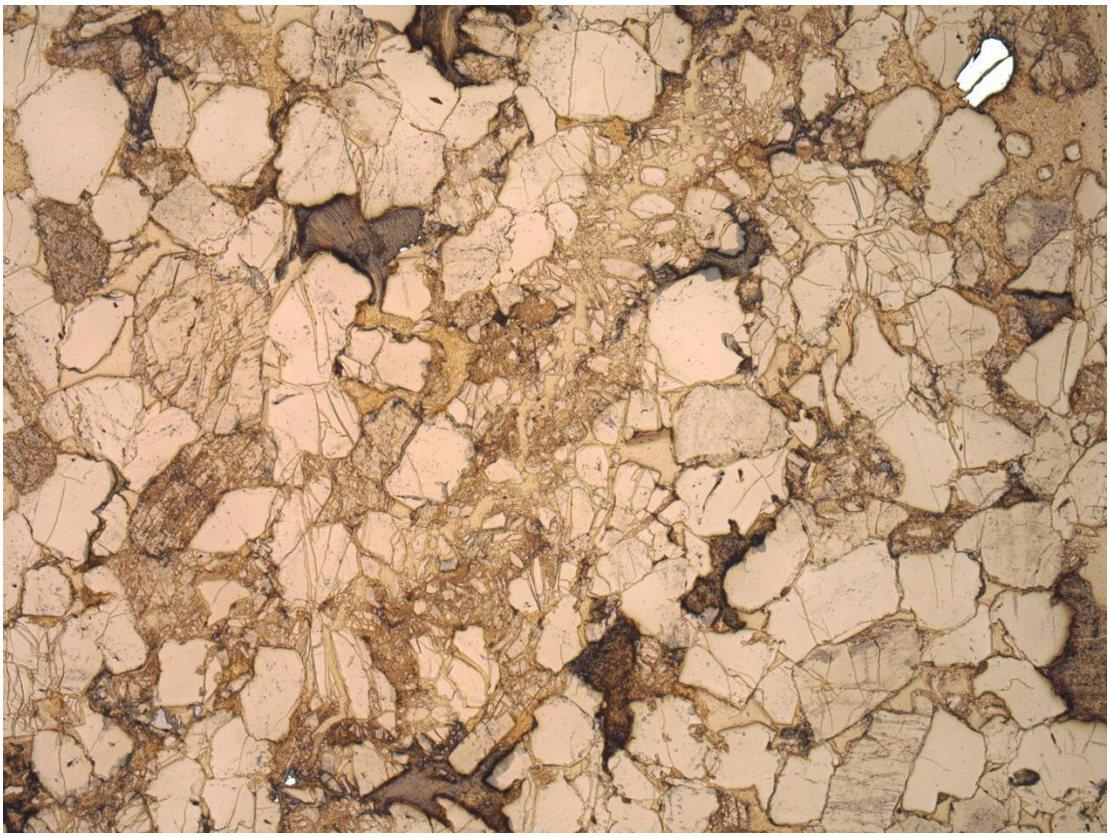

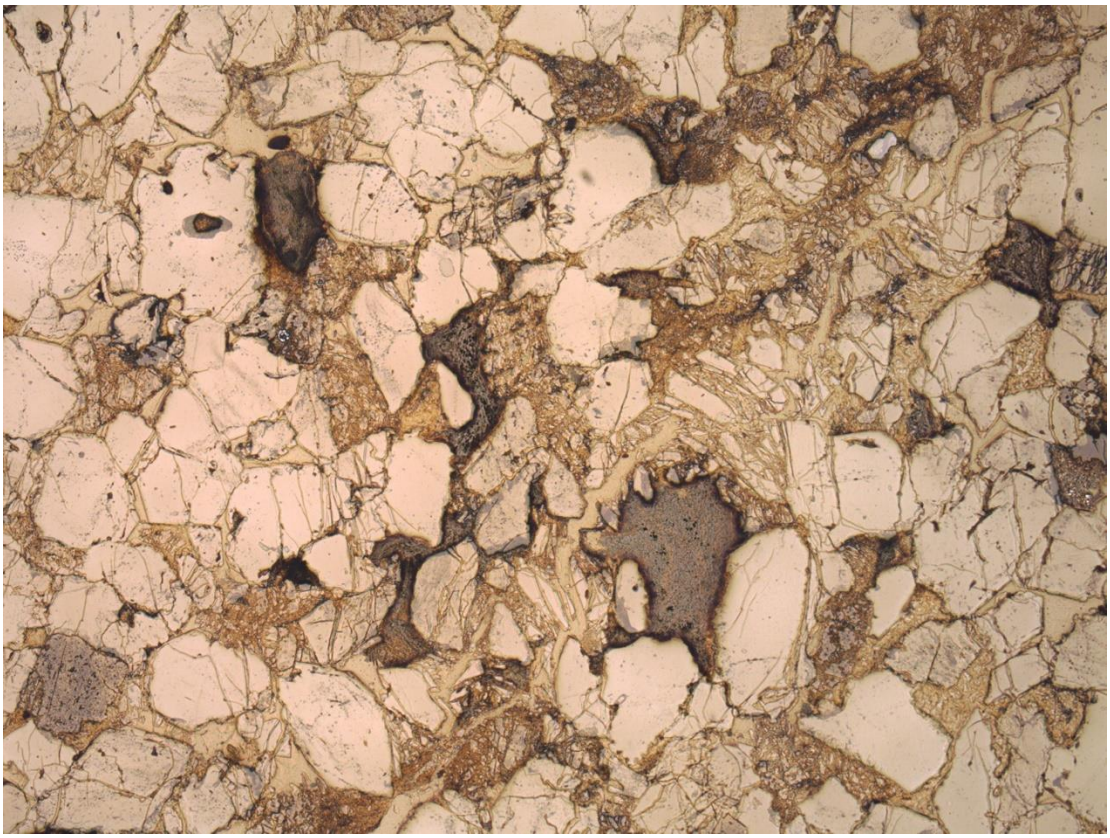

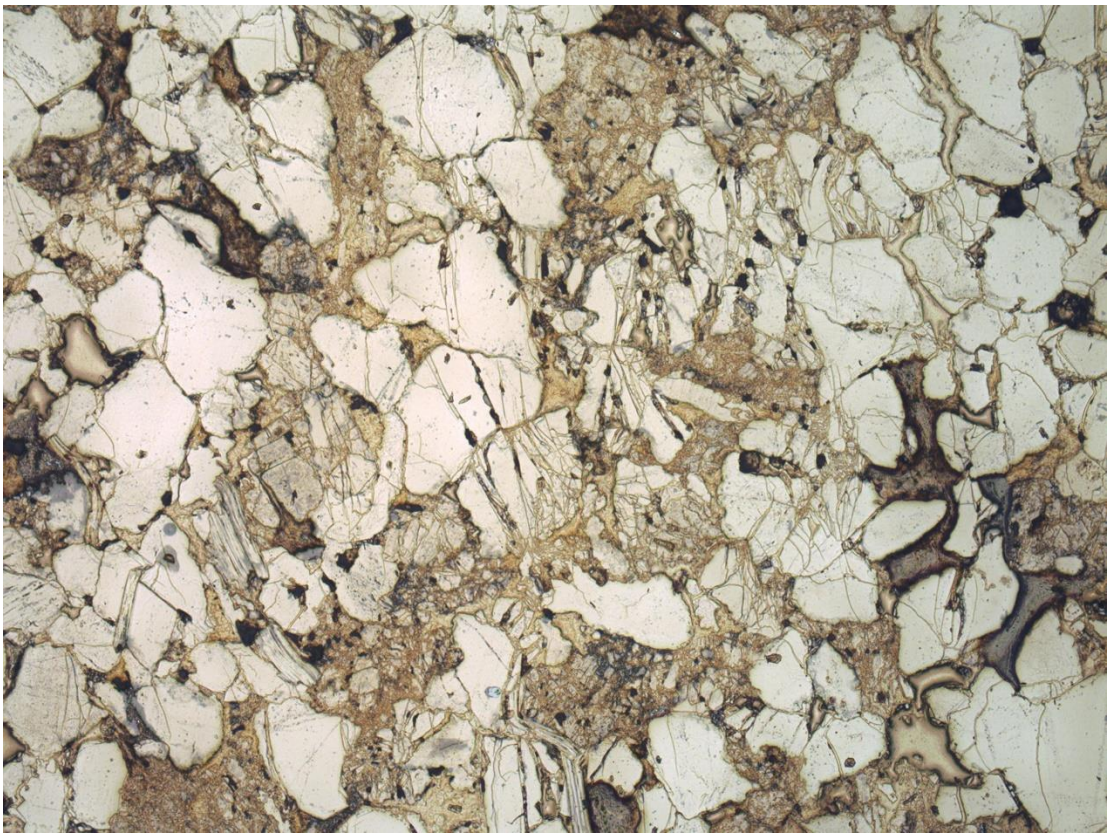

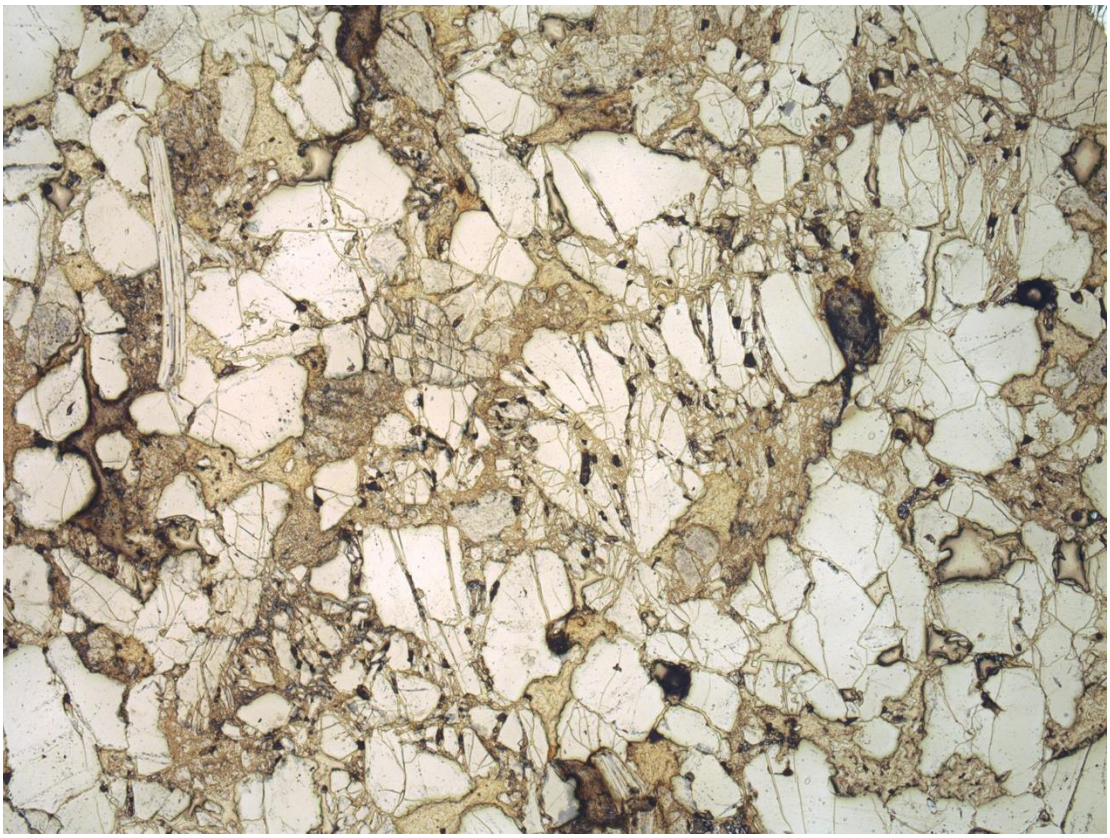

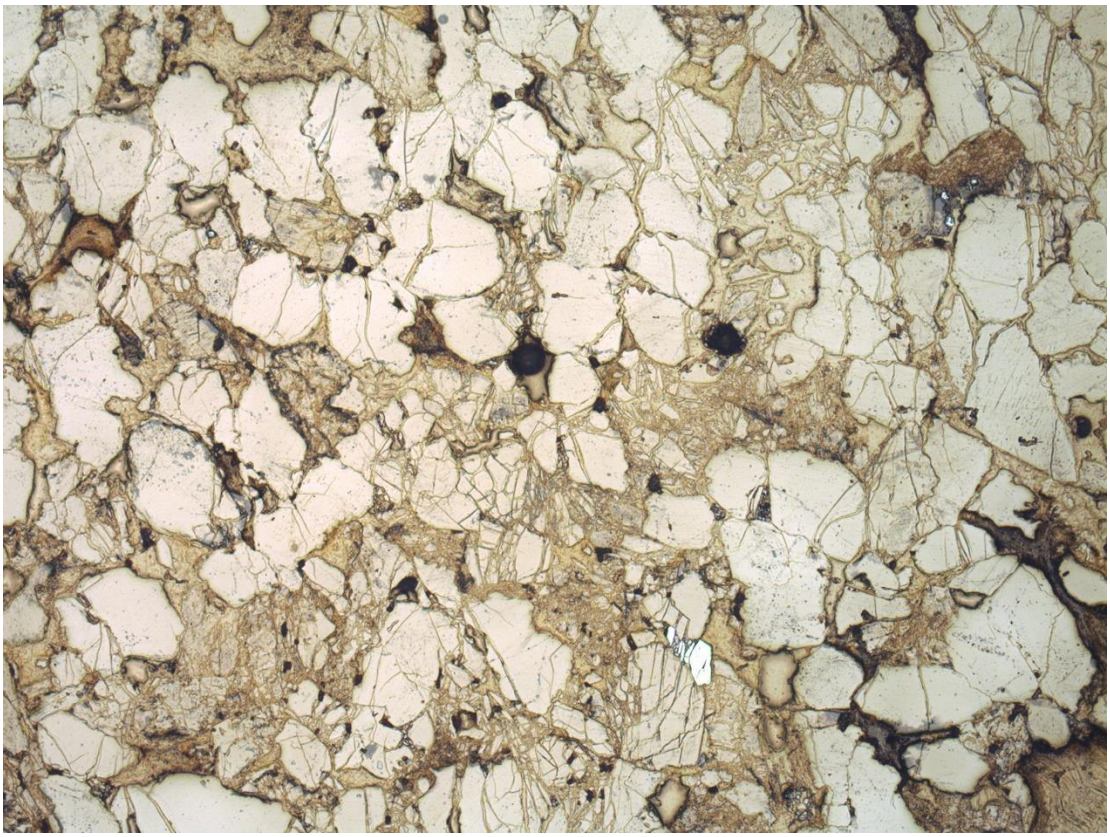

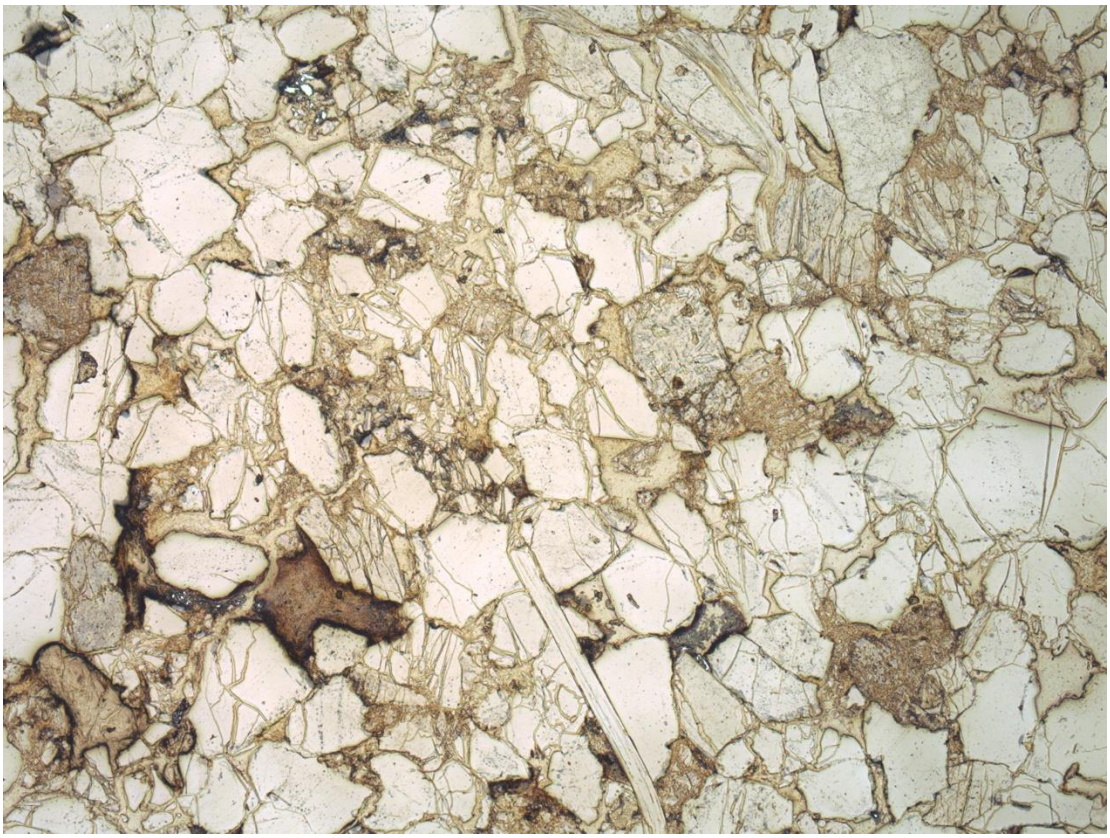

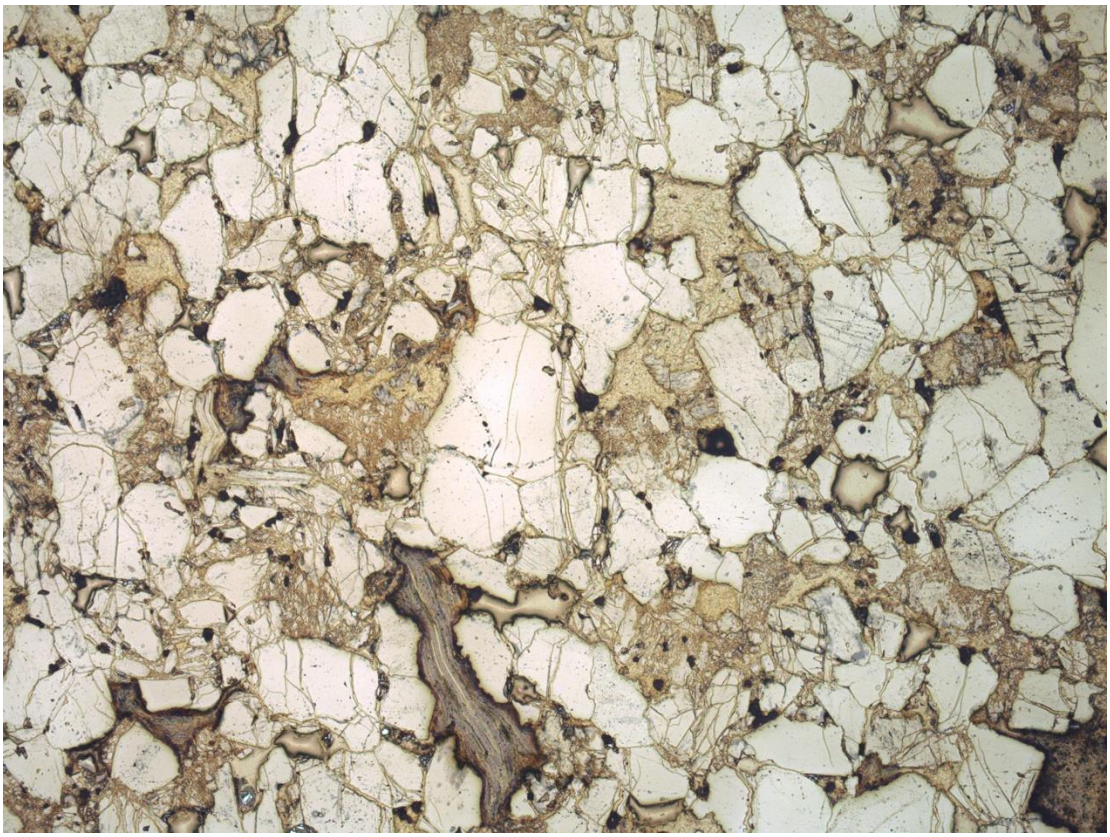

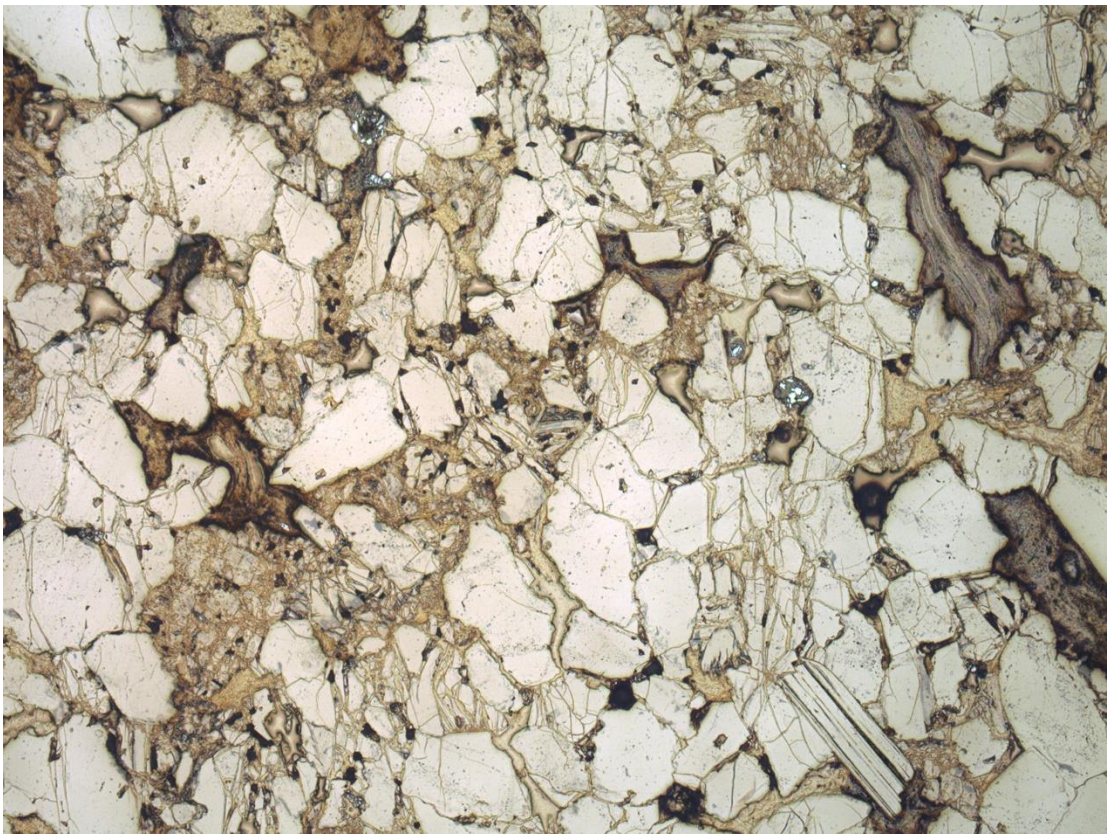

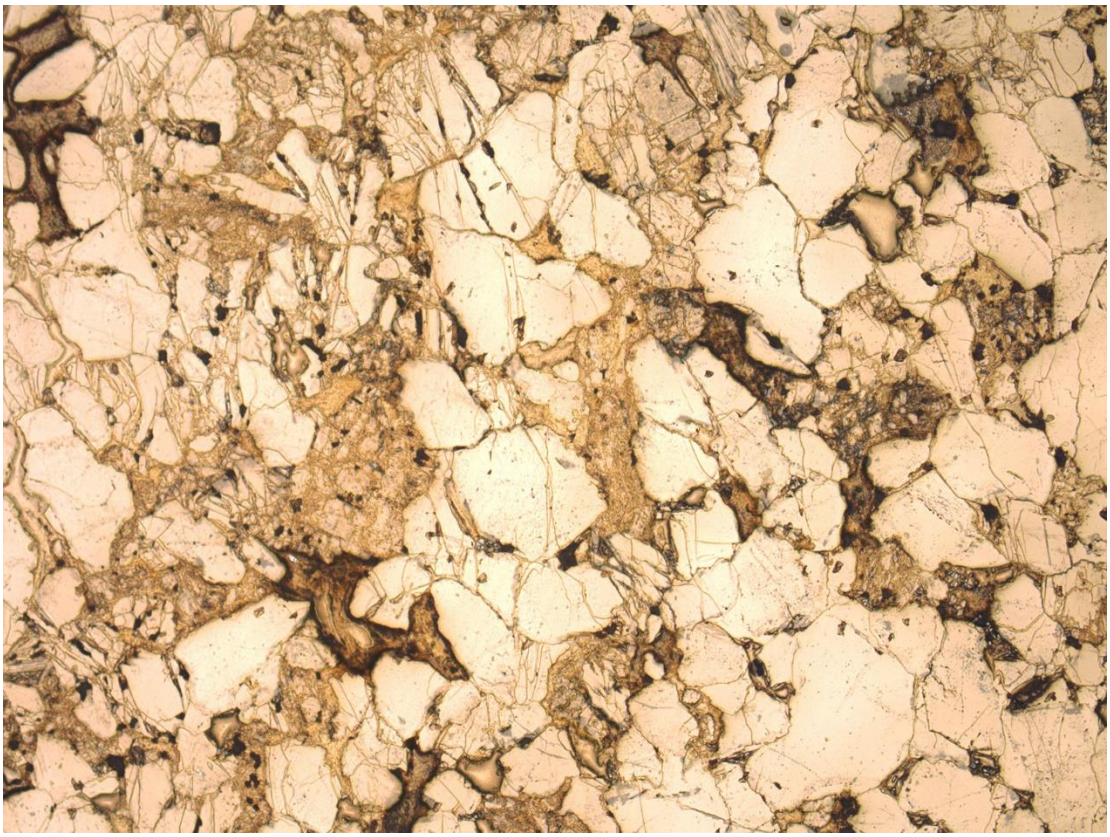

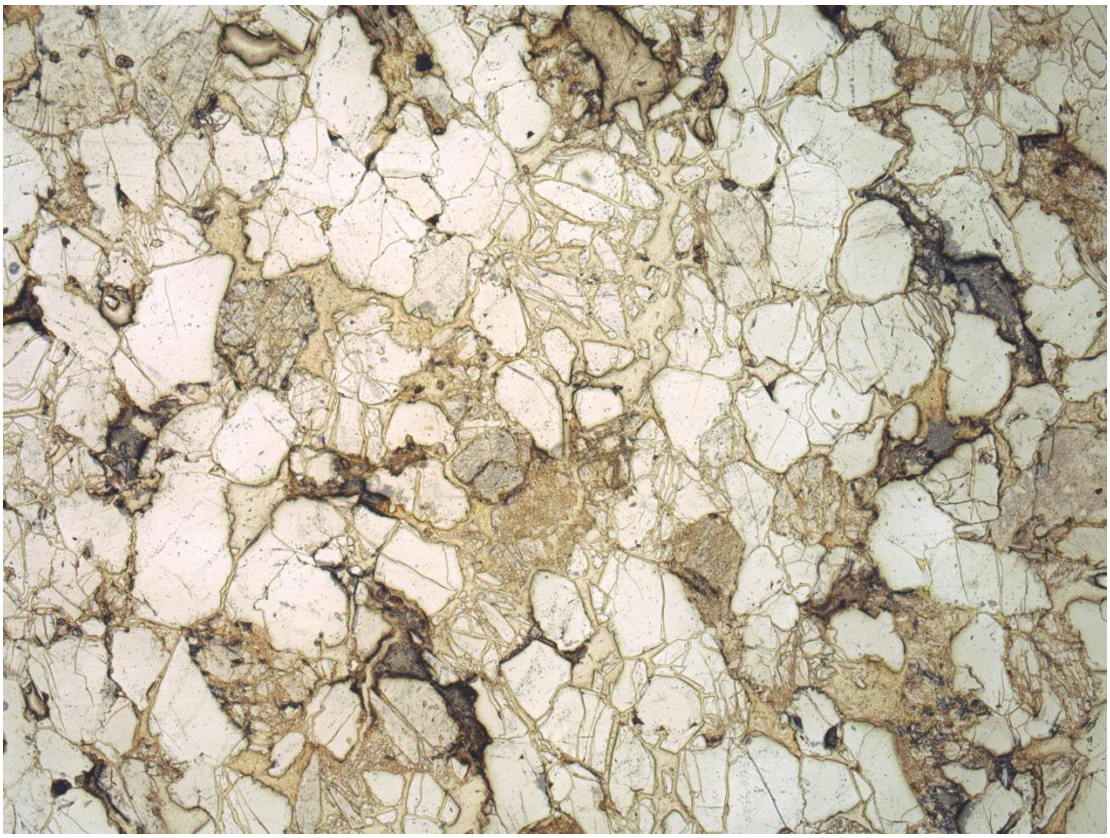

Bibliography

Anderson, O. L., and Grew, P. C. (1977), Stress corrosion theory of crack propagation with applications to geophysics, *Rev. Geophys.*, 15(1), 77– 104, doi:10.1029/RG015i001p00077.

Atkinson, B. K. (1984). Subcritical crack growth in geological materials. *Journal of Geophysical Research: Solid Earth*, *89*(B6), 4077–4114. https://doi.org/10.1029/JB089iB06p04077

Baud, P., & Meredith, P. G. (1997). Damage accumulation during triaxial creep of darley dale sandstone from pore volumometry and acoustic emission. *International Journal of Rock Mechanics and Mining Sciences*, *34*(3), 24.e1-24.e10. https://doi.org/10.1016/S1365-1609(97)00060-9

Baud, Patrick, Zhu, W., & Wong, T. (2000). Failure mode and weakening effect of water on sandstone. *Journal of Geophysical Research: Solid Earth*, *105*(B7), 16371–16389. https://doi.org/10.1029/2000JB900087

Beeler, N. M., Hirth, G., Thomas, A., & Bürgmann, R. (2016). Effective stress, friction, and deep crustal faulting. *Journal of Geophysical Research: Solid Earth*, *121*(2), 1040–1059. https://doi.org/10.1002/2015JB012115

Bilek, S. L., & Lay, T. (2018). Subduction zone megathrust earthquakes. *Geosphere*, *14*(4), 1468–1500. https://doi.org/10.1130/GES01608.1

Brace, W. F., & Martin, R. J. (1968). A test of the law of effective stress for crystalline rocks of low porosity. *International Journal of Rock Mechanics and*

Mining Sciences & Geomechanics Abstracts, *5*(5), 415–426. https://doi.org/10.1016/0148-9062(68)90045-4

Brace, W. F., Paulding, B. W., & Scholz, C. (1966). Dilatancy in the fracture of crystalline rocks. *Journal of Geophysical Research (1896-1977)*, *71*(16), 3939–3953. https://doi.org/10.1029/JZ071i016p03939

Brantut, N., Heap, M. J., Baud, P., & Meredith, P. (2014). Rate- and strain-dependent brittle deformation of Rocks. *Journal of Geophysical Research: Solid Earth*, *119*. https://doi.org/10.1002/2013JB010448

Duda, M., & Renner, J. (2013). The weakening effect of water on the brittle failure strength of sandstone. *Geophysical Journal International*, *192*(3), 1091–1108. https://doi.org/10.1093/gji/ggs090

Fischer, G. J., & Paterson, M. S. (1992). Chapter 9 Measurement of Permeability and Storage Capacity in Rocks During Deformation at High Temperature and Pressure. In B. Evans & T. Wong (Eds.), *International Geophysics* (Vol. 51, pp. 213–252). Academic Press. https://doi.org/10.1016/S0074-6142(08)62824-7

French, M. E., & Zhu, W. (2017). Slow fault propagation in serpentinite under conditions of high pore fluid pressure. *Earth and Planetary Science Letters*, *473*, 131–140. https://doi.org/10.1016/j.epsl.2017.06.009

Heap, M. J., Baud, P., Meredith, P. G., Bell, A. F., & Main, I. G. (2009). Time-dependent brittle creep in Darley Dale sandstone. *Journal of Geophysical Research: Solid Earth*, *114*(B7). https://doi.org/10.1029/2008JB006212

Kato, A., Obara, K., Igarashi, T., Tsuruoka, H., Nakagawa, S., & Hirata, N. (2012). Propagation of Slow Slip Leading Up to the 2011 Mw 9.0 Tohoku-Oki

Earthquake. *Science*, *335*(6069), 705–708. https://doi.org/10.1126/science.1215141

Kitajima, H., & Saffer, D. M. (2012). Elevated pore pressure and anomalously low stress in regions of low frequency earthquakes along the Nankai Trough subduction megathrust. *Geophysical Research Letters*, *39*(23). https://doi.org/10.1029/2012GL053793

Knipe, R. J. (1989). Deformation mechanisms—Recognition from natural tectonites. *Journal of Structural Geology*, *11*(1), 127–146. https://doi.org/10.1016/0191-8141(89)90039-4

Kodaira, S., Iidaka, T., Kato, A., Park, J.-O., Iwasaki, T., & Kaneda, Y. (2004). High Pore Fluid Pressure May Cause Silent Slip in the Nankai Trough. *Science*, *304*(5675), 1295–1298. https://doi.org/10.1126/science.1096535

Koulali, A., McClusky, S., Wallace, L., Allgeyer, S., Tregoning, P., D'Anastasio, E., & Benavente, R. (2017). Slow slip events and the 2016 Te Araroa Mw 7.1 earthquake interaction: Northern Hikurangi subduction, New Zealand. *Geophysical Research Letters*, *44*(16), 8336–8344. https://doi.org/10.1002/2017GL074776

Lei, X., Tamagawa, T., Tezuka, K., & Takahashi, M. (2011). Role of drainage conditions in deformation and fracture of porous rocks under triaxial compression in the laboratory. *Geophysical Research Letters*, *38*(24). https://doi.org/10.1029/2011GL049888

Liu, J., Walter, J. M., & Weber, K. (2002). Fluid-enhanced low-temperature plasticity of calcite marble: Microstructures and mechanisms. *Geology*, *30*(9), 787–790. https://doi.org/10.1130/0091-7613(2002)030<0787:FELTPO>2.0.CO;2

Lloyd, G. E., & Knipe, R. J. (1992). Deformation mechanisms accommodating faulting of quartzite under upper crustal conditions. *Journal of Structural Geology*, *14*(2), 127–143. https://doi.org/10.1016/0191-8141(92)90052-X

Makhnenko, R. Y., & Labuz, J. F. (2015). Dilatant hardening of fluid-saturated sandstone. *Journal of Geophysical Research: Solid Earth*, *120*(2), 909–922. https://doi.org/10.1002/2014JB011287

Martin, R. J. (1980). Pore pressure stabilization of failure in westerly granite. *Geophysical Research Letters*, *7*(5), 404–406. https://doi.org/10.1029/GL007i005p00404

Menéndez, B., Zhu, W., & Wong, T.-F. (1996). Micromechanics of brittle faulting and cataclastic flow in Berea sandstone. *Journal of Structural Geology*, *18*(1), 1–16. https://doi.org/10.1016/0191-8141(95)00076-P

Newman, J., & Mitra, G. (1994). Fluid-influenced deformation and recrystallization of dolomite at low temperatures along a natural fault zone, Mountain City window, Tennessee. *GSA Bulletin, 106*(10), 1267–1280. https://doi.org/10.1130/0016-7606(1994)106<1267:FIDARO>2.3.CO;2

Ougier-Simonin, A., & Zhu, W. (2013). Effects of pore fluid pressure on slip behaviors: An experimental study. *Geophysical Research Letters*, *40*(11), 2619–2624. https://doi.org/10.1002/grl.50543

Ougier-Simonin, A., & Zhu, W. (2015). Effect of pore pressure buildup on slowness of rupture propagation. *Journal of Geophysical Research: Solid Earth*, *120*(12), 7966–7985. https://doi.org/10.1002/2015JB012047

Paterson, M. S., & Wong, T. (Eds.). (2005). Evolution of Physical Properties during Brittle Failure. In *Experimental Rock Deformation—The Brittle Field* (pp. 59–114). Springer. https://doi.org/10.1007/3-540-26339-X_5

Peacock, S. M., Christensen, N. I., Bostock, M. G., & Audet, P. (2011). High pore pressures and porosity at 35 km depth in the Cascadia subduction zone. *Geology*, *39*(5), 471–474. https://doi.org/10.1130/G31649.1

Peng, Z., & Gomberg, J. (2010). An integrated perspective of the continuum between earthquakes and slow-slip phenomena. *Nature Geoscience*, *3*(9), 599–607. https://doi.org/10.1038/ngeo940

Radiguet, M., Cotton, F., Vergnolle, M., Campillo, M., Walpersdorf, A., Cotte, N., & Kostoglodov, V. (2012). Slow slip events and strain accumulation in the Guerrero gap, Mexico. *Journal of Geophysical Research: Solid Earth*, *117*(B4). https://doi.org/10.1029/2011JB008801

Reches, Z., & Lockner, D. A. (1994). Nucleation and growth of faults in brittle rocks. *Journal of Geophysical Research: Solid Earth*, *99*(B9), 18159–18173. https://doi.org/10.1029/94JB00115

Reid, H.F. (1910) Mechanics of the earthquake, the California Earthquake of April 18, 1906. Report of the State Investigation Commission, Carnegie Institution of Washington, Washington DC.

Renard, F., Bernard, D., Desrues, J., & Ougier-Simonin, A. (2009). 3D imaging of fracture propagation using synchrotron X-ray microtomography. *Earth and Planetary Science Letters*, *286*, 285–291. https://doi.org/10.1016/j.epsl.2009.06.040

Renard, F., Cordonnier, B., Kobchenko, M., Kandula, N., Weiss, J., & Zhu, W. (2017). Microscale characterization of rupture nucleation unravels precursors to faulting in rocks. *Earth and Planetary Science Letters*, *476*, 69–78. https://doi.org/10.1016/j.epsl.2017.08.002

Reyners, M., & Bannister, S. (2007). Earthquakes triggered by slow slip at the plate interface in the Hikurangi subduction zone, New Zealand. *Geophysical Research Letters*, *34*(14). https://doi.org/10.1029/2007GL030511

Rice, J. (1980). *The mechanics of earthquake rupture*. *78*.

Rice, J. R. (1975). On the stability of dilatant hardening for saturated rock masses. *Journal of Geophysical Research (1896-1977)*, *80*(11), 1531–1536. https://doi.org/10.1029/JB080i011p01531

Rudnicki, J. W. (1984). Effects of dilatant hardening on the development of concentrated shear deformation in fissured rock masses. *Journal of Geophysical Research: Solid Earth*, *89*(B11), 9259–9270. https://doi.org/10.1029/JB089iB11p09259

Rudnicki, John W., & Chen, C.-H. (1988). Stabilization of rapid frictional slip on a weakening fault by dilatant hardening. *Journal of Geophysical Research: Solid Earth*, *93*(B5), 4745–4757. https://doi.org/10.1029/JB093iB05p04745

Saffer, D. M., & Tobin, H. J. (2011). Hydrogeology and Mechanics of Subduction Zone Forearcs: Fluid Flow and Pore Pressure. *Annual Review of Earth and Planetary Sciences*, *39*(1), 157–186. https://doi.org/10.1146/annurev-earth-040610-133408

Shelly, D. R., Beroza, G. C., Ide, S., & Nakamula, S. (2006). Low-frequency earthquakes in Shikoku, Japan, and their relationship to episodic tremor and slip. *Nature*, *442*(7099), 188–191. https://doi.org/10.1038/nature04931

Solomon, E. A., Kastner, M., Wheat, C. G., Jannasch, H., Robertson, G., Davis, E. E., & Morris, J. D. (2009). Long-term hydrogeochemical records in the oceanic basement and forearc prism at the Costa Rica subduction zone. *Earth and Planetary Science Letters*, *282*(1), 240–251. https://doi.org/10.1016/j.epsl.2009.03.022

Terzaghi, K. (1943) Theoretical Soil Mechanics. Wiley, New York.

Tobin, H. J., & Saffer, D. M. (2009). Elevated fluid pressure and extreme mechanical weakness of a plate boundary thrust, Nankai Trough subduction zone. *Geology*, *37*(8), 679–682. https://doi.org/10.1130/G25752A.1

Uchida, N., Shimamura, K., Matsuzawa, T., & Okada, T. (2015). Postseismic response of repeating earthquakes around the 2011 Tohoku-oki earthquake: Moment increases due to the fast loading rate. *Journal of Geophysical Research: Solid Earth*, *120*(1), 259–274. https://doi.org/10.1002/2013JB010933

Underwood, E. E. (1969). Stereology, or the quantitative evaluation of microstructures. *Journal of Microscopy*, *89*(2), 161–180. https://doi.org/10.1111/j.1365-2818.1969.tb00663.x

Walsh, J. B. (1965), The effect of cracks on the compressibility of rock, *J. Geophys. Res.*, 70(2), 381– 389, doi:10.1029/JZ070i002p00381.

Wong, T. (1982). Shear fracture energy of Westerly granite from post-failure behavior. *Journal of Geophysical Research: Solid Earth*, *87*(B2), 990–1000. https://doi.org/10.1029/JB087iB02p00990

Wong, T., David, C., & Zhu, W. (1997). The transition from brittle faulting to cataclastic flow in porous sandstones: Mechanical deformation. *Journal of Geophysical Research: Solid Earth*, *102*(B2), 3009–3025. https://doi.org/10.1029/96JB03281

Wu, X. Y., Baud, P., & Wong, T. (2000). Micromechanics of compressive failure and spatial evolution of anisotropic damage in Darley Dale sandstone. *International Journal of Rock Mechanics and Mining Sciences*, *37*(1), 143–160. https://doi.org/10.1016/S1365-1609(99)00093-3

Zhu, W., & Wong, T. (1997). The transition from brittle faulting to cataclastic flow: Permeability evolution. *Journal of Geophysical Research: Solid Earth*, *102*(B2), 3027–3041. https://doi.org/10.1029/96JB03282